Computational Modelling of Blood Flow in Sickle Cell Disease

Leszek Kazimierz Wierzchleyski

UCL

Department of Mathematics

Supervised by Dr Philip Pearce and Prof Helen Wilson

A thesis presented for the degree of

Master of Philosophy

I, Leszek Kazimierz Wierzchleyski confirm that the work presented in my thesis is my own. Where information has been derived from other sources, I confirm that this has been indicated in the thesis.

First and foremost I would like to thank my supervisors, Dr Philip Pearce and Prof Helen Wilson. They have both been absolutely fantastic in terms of the support which they have given me, both academic and otherwise. They have allowed me to pursue my interests and not tried to force their interests onto me. This project would not have been possible without their hard work and dedication

Second I would like to thank our IT technicians, Mr Richard Hoyle and Mr Ibrahim Bulime. This was a highly computational project, which simply would not have been possible without their support. They compiled the code for me on the department cluster and were always available for troubleshooting and technical support.

Third I would like to thank my collaborator Prof Timm Kruger. He is responsible for the BioFM code itself and has always been willing to provide consultation.

Finally I would like to thank my experimental collaborators Dr David Wood and Ms Hannah Szafraniec. I have very much enjoyed working with them.

I would like to dedicate this thesis to Dr Angelo Grubisic (1981-2019). My tutor, mentor and friend.

Abstract

Sickle Cell Disease is a genetic condition in which red blood cells become stiff and misshapen. This in turn causes blockages in blood vessels which leads to oxygen deprivation to different organs, with potentially lethal consequences. Recent experimental observations have shown significant heterogeneity in the properties of red blood cells within blood samples from patients with Sickle Cell Disease. Here, we investigate how such cell property distributions lead to different blood flow rheologies. We show that in mixtures of stiffened and healthy cells, stiffer cells tend to migrate towards vessel walls, in agreement with previous findings. Furthermore, we investigate the role of cell shape in homogeneous mixtures of cells. We find that stiffened cells which retain a biconcave disc shape lead to a higher effective blood flow viscosity than those which deform into a spherical shape; this contrasts with deformable cells, which show the opposite behaviour. We suggest that this is because when stiffened, biconcave cells tend to lie closer to the vessel wall than spherical cells, and thus increase effective friction. These results inform our understanding of how cell stiffness and shape affect blood rheology in Sickle Cell Disease.

Impact Statement

Sickle Cell Disease is one of the most common genetic diseases and as such working towards a greater understanding of this disease and ultimately a cure will improve human health in the long term. The key result of this thesis gives an insight as to how red blood cell geometry in Sickle Cell Disease can have a significant impact on blood flow rheology. If this research is extended, it could reveal how red blood cell geometry effects clinical signatures in Sickle Cell Disease.

Contents

1 Introduction **1**

2 Background **3**

2.1 Sickle Cell Disease . . . 3

2.2 Haemodynamics . . . 6

2.2.1 Poiseuille Flow . . . 10

2.2.2 Shear-Thinning Fluids . . . 12

2.3 Einstein Viscosity . . . 14

3 Methods **15**

3.1 Converting Between Simulation and Dimensional Units . . . 16

3.1.1 Size Scaling . . . 16

3.1.2 Time Scaling . . . 16

3.1.3 Stiffness Scaling . . . 17

3.1.4 Pressure Gradient . . . 18

3.2 Numerical Checks . . . 19

3.3 Plotting . . . 20

3.4 Immersed Boundary Method . . . 21

3.4.1 Algorithm . . . 21

3.4.2 Membrane Model . . . 22

4 Dilute Flow **23**

5 SCD Blood Flow **27**

6 Conclusion **37**

6.1 Conclusions . . . 37

6.2 Future Work . . . 38

7 References **38**

1 Introduction

The purpose of this thesis is to explore the biomechanics of Sickle Cell Disease (SCD) through computational blood flow modelling, resolved at the cellular scale. At a high level, SCD is a genetic condition in which red blood cells (RBCs) become rigid and misshapen. This causes them to form a blockage known as vaso-occlusion, which in turn cuts off blood flow and can cause extreme pain, stroke and in the worst cases, organ failure [11].

For a long time it was thought that RBCs affected by SCD would have a crescent shape and would all have the same stiffness value. In recent years, experiments have shown a high level of heterogeneity in terms of cell property distributions (stiffness and shape) in SCD [16]. Despite decades of intense research, it is not known how cell properties determine emergent blood rheology and disease outcomes in SCD patients.

Work has already been done on how cell shape can affect the velocity of a single cell. It has been observed that sickled cells with a crescent shape move with higher velocity than sickled cells with a biconcave disc shape [3]. It has been suggested that this is due to the fact that crescent shaped cells align themselves with the direction of flow and as such cross fewer streamlines. Cells which travel parallel to the direction of flow are likely to cause a transient blockage, but if the cell turns perpendicular to the flow then it is likely to cause a persistent blockage and as such is more dangerous. It has been observed that cells are more likely to turn perpendicular to the direction of flow if they are close to other cells as this subjects them to an additional velocity gradient [1]. Shape has also been observed to play a role in the likelihood of vaso-occlusion. Crescent shaped sickled cells are less adhesive than biconcave disc shaped sickled cells. However the crescent shaped cells are more likely to be trapped by the highly adhesive white blood cells [4]. This means that different shapes can be dangerous in different ways. As well as the shape of the cells, the geometry of the vasculature has been shown to have an impact on vaso-occlusion. Vaso-occlusion is most likely to happen near a bifurcation. This is because eddies form near bifurcations and this increases the amount of time RBCs spend in this area [2].

The importance of cell stiffness has also been studied. Stiff cells experience a smaller lifting force from the vessel walls than more flexible ones [14]. This means that they migrate closer to the vessel walls in a process called margination. This in turn reduces the thickness of the cell free layer (a layer of blood plasma which acts as a lubrication layer) and thus increases the friction in the system [5]. This occurs in situations where there are a mixture of rigid cells and healthy cells. Stiffness affects RBC dynamics more generally as well, with flexible RBCs undergoing slippering (where they align themselves with the flow and stretch into an ellipsoid shape) or parachuting (where they are perpendicular to the flow and the rim of the cell folds backwards) [7]. This allows them to cross fewer streamlines and move through the plasma more efficiently. This becomes more difficult as cells become stiffer and are less able to morph into these shapes. Additionally it has been observed that SCD causes an increase in the production of cytokines. These are proteins which

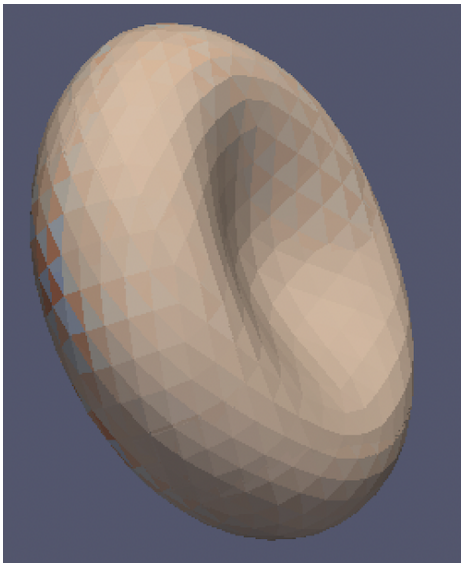

Figure 1: Example of a red blood cell with a biconcave disc shape.

control the growth of blood cells. The excessive production of cytokines in SCD leads to increased cell adhesiveness and thus further contributes to vaso-occlusion [15].

We shall now look more broadly at suspension flow mechanics and jamming. In a dilute regime - namely a volume fraction of 3 percent or less, there is a linear relationship between volume fraction and effective viscosity. Einstein reasoned that if infinitely rigid spheres are suspended in a fluid, such that the radius of the spheres is much smaller than the radius of the vessel (ideally an infinite ratio) and the spaces between the spheres is much larger than the radii of the spheres, then the spheres will resist the shear force from the background fluid and as such each one will add a contribution to the effective viscosity of the fluid [8]. Einstein viscosity has been extended beyond the dilute limit, by including a non-linear term [12]. In more dense suspensions it has been found that as the aspect ratio of the particles is increased, the effective viscosity of the fluid decreases [10]. This links in with the aforementioned idea that crescent shaped sickled cells flow at a higher velocity than biconcave disc shaped sickled cells. It is worth noting that there is a considerable lack of literature on how particle stiffness affects effective viscosity in general suspension flow mechanics.

At higher volume fractions in solid suspensions, we may see jamming occurring. This is where solid particles can know longer move past each other or rearrange and it is similar to vaso-occlusion [13]. The geometry of particles changes the critical volume fraction at which jamming occurs. As aspect ratio increases the critical jamming fraction decreases [9]. This is relevant as it links in with the fact that some sickled cells have a crescent shape and thus a high aspect ratio. The reason that critical jamming fraction decreases as particle aspect ratio increases, is because there are a greater number of random contacts between particles of greater aspect ratio [9]. Maxwell reasoned that the number of contacts per particle required for a structure to remain intact (and hence cause a jam) is six.

In this thesis we shall study how different RBC properties affect blood flow rheology, as well as how heterogeneity in RBC property distributions affect blood flow rheology. This thesis is structured as follows. Chapter 2 gives an in depth background in haemodynamics, sickle cell disease and Einstein viscosity. Chapter 3 describes the methods we have used and how simulations are set up. Chapter 4 looks at the results of simulations of dilute flows. Chapter 5 looks at the results of simulations of blood flow (both healthy and SCD). The final chapter is the conclusion.

2 Background

2.1 Sickle Cell Disease

In 1910 Dr James Herrick was seeing a patient who was complaining of episodes of extreme pain. Upon viewing a sample of the patients blood under a microscope, Dr Herrick noticed that some of the RBCs in the sample had a crescent or sickle like shape, instead of a biconcave disc shape[18]. Dr Herrick concluded that the misshapen RBCs must be getting caught in the blood vessels and thus inhibiting flow (vaso-occlusion) and depriving parts of the body of oxygen. This would explain the extreme pain and potentially also lead to major complications. He coined the term Sickle Cell Disease (SCD) to describe the condition.

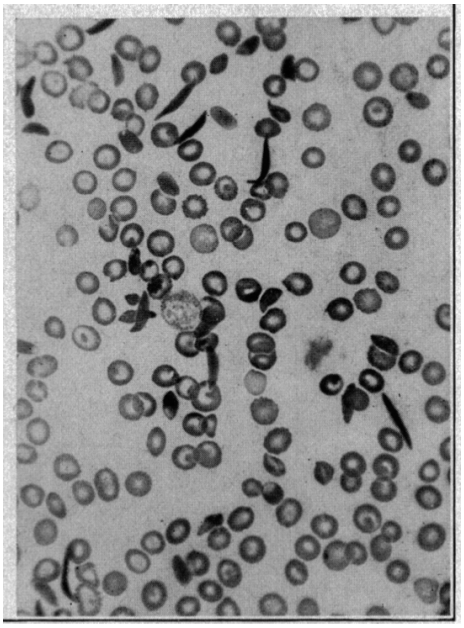

Figure 2: The blood sample of the first recorded SCD patient under a microscope[18]

In later years it was discovered that RBCs in SCD are far more rigid than healthy RBCs[3]. It stood to reason that this must also be part of the problem, because as previously mentioned RBCs sometimes have to deform to pass through small blood vessels or to move past other RBCs and this becomes impossible if the RBC is too stiff. Initially this idea encountered a lot of resistance, but it was eventually accepted that stiffness played a role in SCD alongside shape. It is worth noting that the upper bound of stiffness for sickled cells is unknown and this is one of things we will investigate

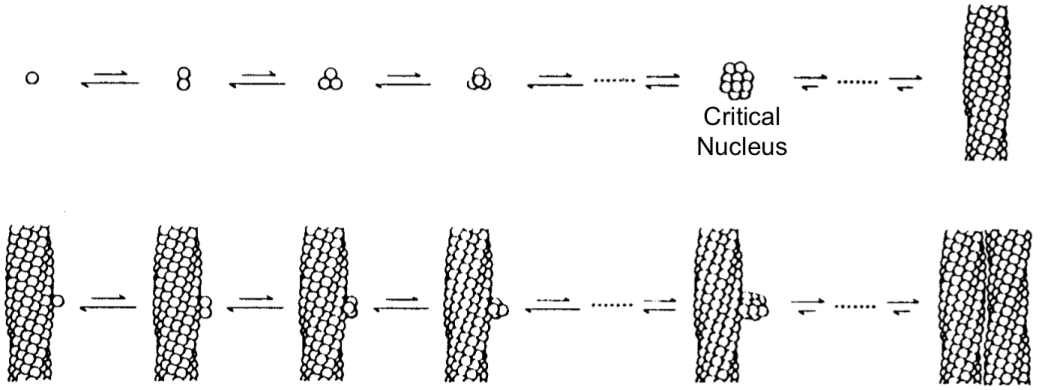

Figure 3: Schematic showing an example of a haemoglobin polymerisation process in SCD[30]

in this project.

SCD is a genetic disease in which haemoglobin molecules inside an affected RBC aggregate into a polymer[30]. This is what causes the membrane to become misshapen and the cell to become stiff. This occurs under conditions of low oxygen tension (partial oxygen pressure in the blood) and thus does not generally occur in the arteries (save for the pulmonary artery). SCD predominately affects people of African or Caribbean ethnicity. This is not a coincidence. The gene mutation that causes SCD occurs in the HBB gene. A Thymine base replaces an Adenine base and coverts the HBB gene to an HbSS gene. This gene gives some protection against Malaria (hence it evolved primarily in Africa and the Caribbean), but if both parents have this gene then each of their offspring have a 25 percent chance of being born with SCD[11].

SCD is a very harmful disease, with an average life expectancy of just 54 years. This is largely because of the severe pathologies associated with SCD, such as stroke, acute chest syndrome, renal failure and pulmonary hypertension [6]. A number of treatments exist to help alleviate the complications associated with SCD. Blood transfusions are the primary method for treating and preventing vaso-occlusive crises. It is not known how to optimise blood transfusions based on individual patient needs. Bone marrow transplants are the only known cure, but this procedure can only be used in a fraction of cases and has associated complications. There are a number of experimental treatments in development, both genetic and pharmaceutical. Gene therapy is a very exciting possibility for treating SCD. Broadly speaking there are four different types of gene therapy which are being studied for SCD. The first is gene addition, in which a non-sickling haemoglobin gene is added to the patient's stem cells using a viral vector. This produces new healthy haemoglobin in addition the sickling haemoglobin (it doesn't replace it). The second method is gene editing. The production of fetal haemoglobin (HbF) is suppressed after birth. HbF cannot sickle and thus is very useful in treating SCD. Gene editing therapy can target the suppression of HbF production and also reduce the amount of HbS (this is replacement). The third method is called gene silencing. This is somewhat similar to gene editing as it produces HbF and suppresses HbS through gene regulation.

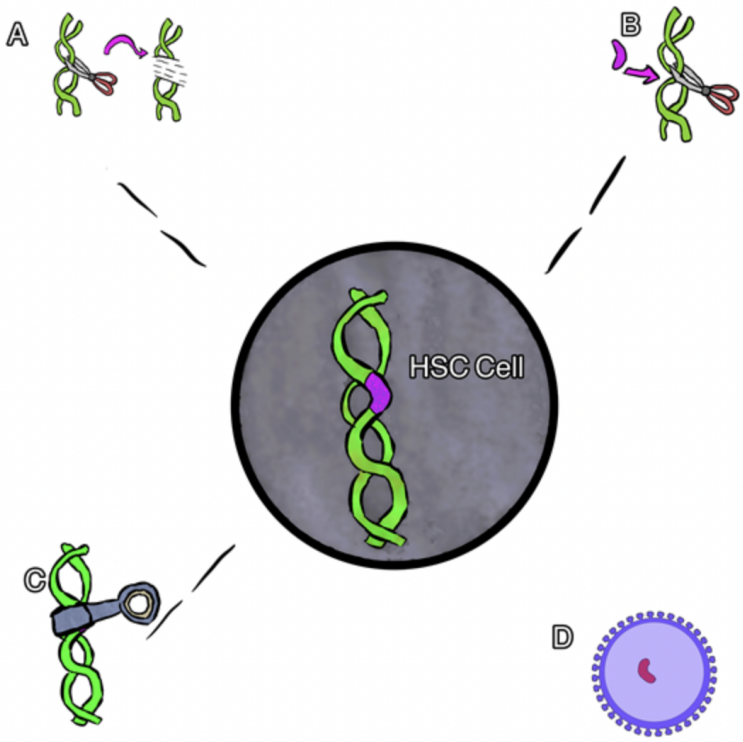

Figure 4: Cartoon rendering of different gene therapies. (A) Gene editing, (B) gene correction, (C) gene silencing, and (D) gene addition via viral vector.[29]

The difference is that it uses a viral vector as a delivery method. Finally we have gene correction, in which an RNA molecule is used to locate the mutation in question and it is then cut and a DNA template is put in place. This removes sickle haemoglobin and produces non-sickle haemaglobin[7]. On the pharmaceutical side there are a number drugs in use, including Hydroxyurea, L-glutamine oral powder and Crizanlizumab. These medications reduce the frequency of Sickle Cell Crises, but do not cure the disease itself. Voxelotor can reduce the chance of anemia and improve blood flow. Voxeletor has shown promising results in preventing HbS from sickling and as such may actually work to counteract the underlying mechanism of SCD[29].

For a long time a very homogeneous view of SCD was held, in which affected RBCs would all reach a maximum possible stiffness value and would all take the form of the classic sickle shape. Experiments in recent years have shown that this is not the case and in fact affected RBCs can have a range of shapes and stiffness values[9]. This means that SCD exhibits an unexpectedly high level of heterogeneity. This level of heterogeneity means that a one size fits all approach to treating SCD would not be ideal and thus the disease is a prime candidate for the practice of personalised medicine. In personalised medicine a patient has their treatment plan tailored to them based on their genetics, computational models of their physiology based on medical imaging, and lab results.

Figure 5 shows how drastically the shapes of RBCs in a sample of sickle cell blood can vary. Given that different shapes have different jamming fractions when suspended in flow and that dif-

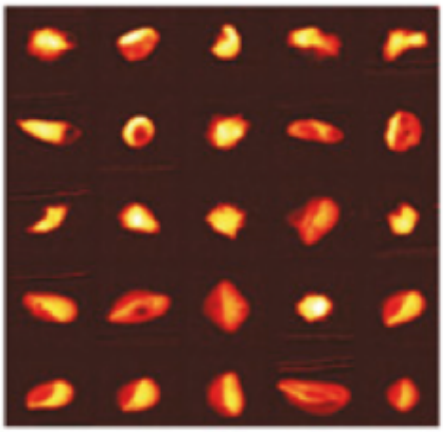

Figure 5: Sample of RBCs from a patient with SCD. It demonstrates the heterogeneity in SCD[16]

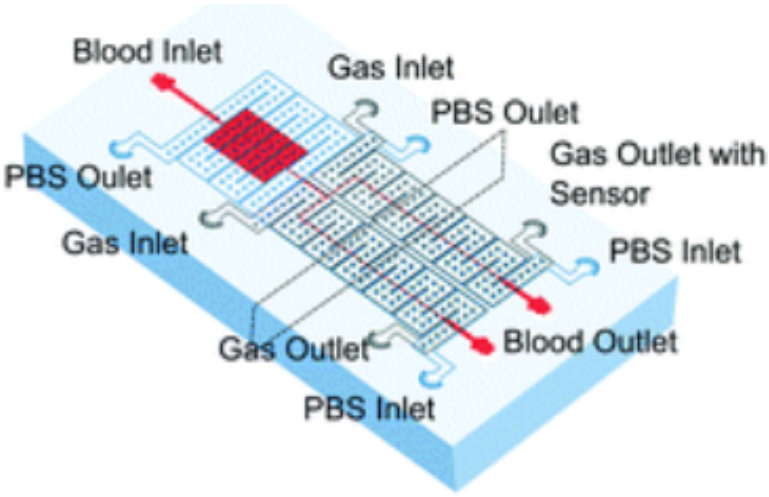

Figure 6: Schematic of the micro-fluidic device used by our collaborators[16]

ferent shapes lead to different effective viscosities, this shape heterogeneity is important in blood flow rheology.

We are working with experimental collaborators. They are running an experiment in which a sample of RBCs from an SCD patient are suspended in a saline solution and passed through a micro-fluidic device with a square channel. The channel is deoxygenated and the cells are filmed with a high-speed camera and inverted bright field microscope. The cells are tracked using a feature tracking algorithm such that flow profiles can be extracted[16]. Our experimental collaborators are Dr David Wood who is the head of the lab and the principal investigator and Ms Hannah Szafraniec (Dr Wood's PhD student) who is running the aforementioned experiments.

2.2 Haemodynamics

Although blood is often thought of as a fluid, this is not quite accurate in the traditional sense of the word. Blood consists of blood plasma (which is a fluid) as well as a number of different types

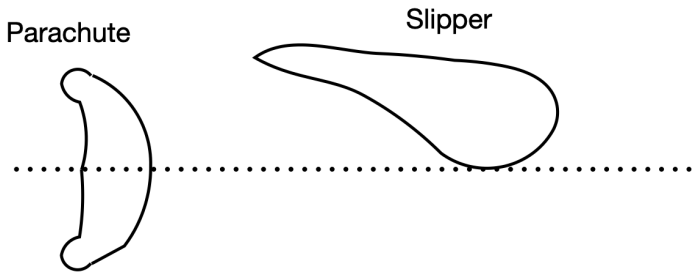

Figure 7: Schematic showing a parachute and slipper RBC

of cells suspended in said fluid. These are red blood cells, white blood cells and platelets. As RBCs have the largest volume fraction by far of any cell type, they are the cell in which we are most interested, because they have the greatest effect on haemodynamics.

Healthy red blood cells (RBCs) are highly flexible with a stiffness value of approximately 5×10^{-6}N/m. This high level of deformability allows them to pass unencumbered through even the smallest blood vessels and it also allows them to move past each other easily, such that a cluster of healthy RBCs won't cause a blockage. At equilibrium an RBC has a biconcave disk shape, but under stress they will morph into a variety of shapes (provided topology is conserved). When flowing through blood vessels, RBCs tend to either parachute - the cell is perpendicular to the flow and the rim of the cell folds backwards, or slipper - the cell is aligned with the flow and stretches to form an ellipsoid shape. Broadly speaking parachuting tends to occur closer to the centre of the vessel and slippering happens closer to the walls of the vessel[20]. This is largely due to the effect of different shear rates and flow velocities throughout the flow profile, but we will discuss this further when we talk about Poiseuille flows. In both of these cases the RBCs reduce their cross sectional area facing the flow and are able to move more efficiently. The key point here is that under normal conditions, healthy RBCs flow efficiently and do not get stuck. This allows them to perform their role of transporting oxygen around the body.

Ellipsoidal cells such as those that have slippered, tend to undergo tank treading[20]. This is where the membrane of the RBC rotates around the cytoplasm inside the cell. As one can imagine, ellipsoidal cells are prone to rolling around their axis instead of flipping end over end as less torque is required to rotate them around the longer axis. This tank treading motion generates lift on the cell causing it to migrate away from the vessel walls. This leads to what is known as the Fåhræus-Lindqvist effect[19]. In narrow blood vessels of less than 0.3mm, a change in diameter leads to a change in effective viscosity. This is because the cells migrate to the centre of the vessel where the fluid velocity is highest and leave a comparatively thick cell free lubrication layer of plasma at the wall. This is an added non-Newtonian effect. It is worth noting that this lifting force is reduced for stiffer cells as this will be important later[14]. Next we shall consider the cell motion known as snaking[20]. This is where an RBC undergoes a periodic oscillatory motion near the centre line of the vessel, which in turn leads to an orbital drift. This mostly occurs at low shear rates. At

higher shear rates we might see tumbling for RBCs which retain something close to their original biconcave disc shape. When the RBC is close to symmetrical, there is no mechanical advantage for the RBC to rotate about a particular axis (like there is in tank treading) and thus the RBCs will just tumble in the direction of flow. For RBCs which have slippered, the expected dynamics at high shear rates is swinging[20]. It is important to understand that different cell dynamics can be expected at different shear rates, because this means that the cell dynamics will be different in blood vessels of different diameters and local pressures.

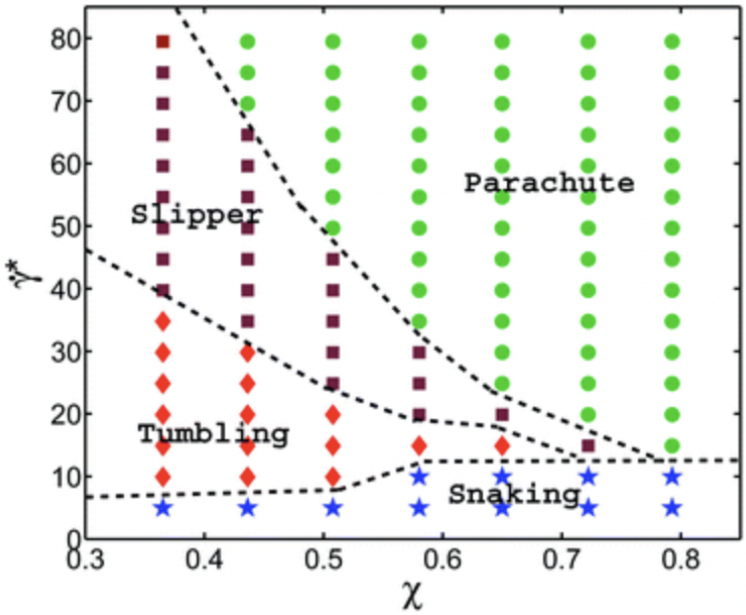

Figure 8: A phase diagram for $\Gamma = 2662$ ($\mathrm{Yr} = 18.9 \times 10^{-6}\ Nm^{-1}$, $\kappa_r = 3 \times 10^{-19}$ J), which mimics average membrane properties of a healthy RBC. The plot shows various RBC dynamics states depending on the flow strength characterized by $\dot{\gamma}^*$ and the confinement χ. The symbols depict performed simulations, with the RBC states: parachute (green circles), slipper (brown squares), tumbling (red diamonds) and snaking (blue stars) discocytes. The phase-boundary lines are drawn schematically to guide the eye[20]

As can be seen in figure 8, we have a good visual representation of some of the concepts discussed so far and how they change with shear rate and confinement. Γ is the Föppl–von Kármán number (more on that later), $\dot{\gamma}^*$ is the non-dimensional shear rate, κ_r is the membrane bending rigidity and confinement (χ) is the ratio of cell radius to vessel radius. At low shear rates the RBCs retain their biconcave disc shapes and have snaking motion. This changes to tumbling at higher shear rates. At even higher shear rates the RBCs no longer retain their biconcave disc shapes, with slippering being more likely at lower confinement and parachuting being more likely at higher confinement.

In SCD the stiffness values of the RBCs change and so it is appropriate to look at how this change in stiffness affects individual cell dynamics.

Figure 9 shows us that at higher stiffness values the transition from biconcave disc shaped RBCs

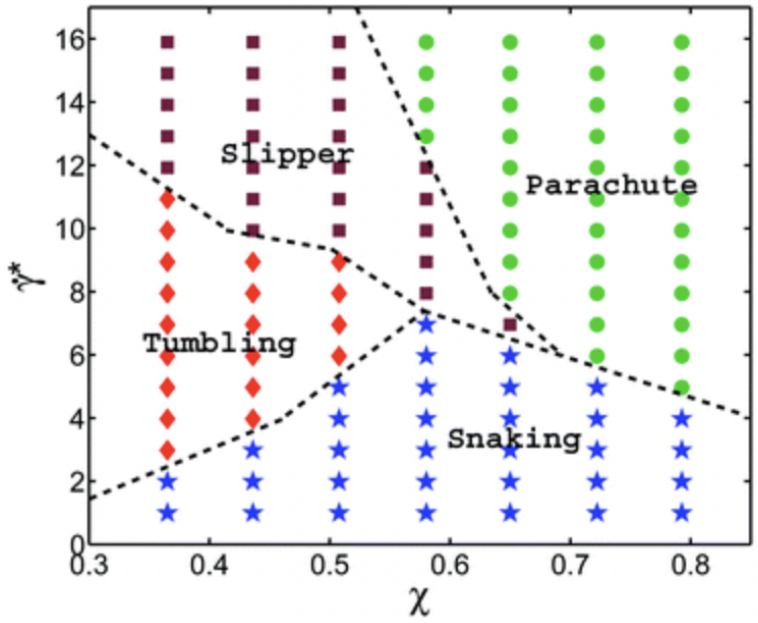

Figure 9: A phase diagram for $\Gamma = 532$ (Yr $= 18.9 \times 10^{-6}\ Nm^{-1}$, κr $= 1.5 \times 10^{-18}$ J), such that the bending rigidity of a cell membrane is five times larger than that of a healthy RBC. The plot shows various RBC dynamics states depending on the flow strength characterized by $\dot{\gamma}^*$ and the confinement χ. The symbols depict performed simulations, with the RBC states: parachute (green circles), slipper (brown squares), tumbling (red diamonds) and snaking (blue stars) discocytes. The phase-boundary lines are drawn schematically to guide the eye[20].

to slipper and parachute shaped RBCs, as well as the transition from snaking to tumbling, happens at a much lower shear rate. It can also be seen that tumbling and slippering do not occur at quite so high confinement levels as they did for healthy RBCs. It is thought that the different cell dynamics seen at different stiffness values are due to the suppression of thermal fluctuations as stiffness is increased[21].

Figures 8 and 9 are produced from simulations.

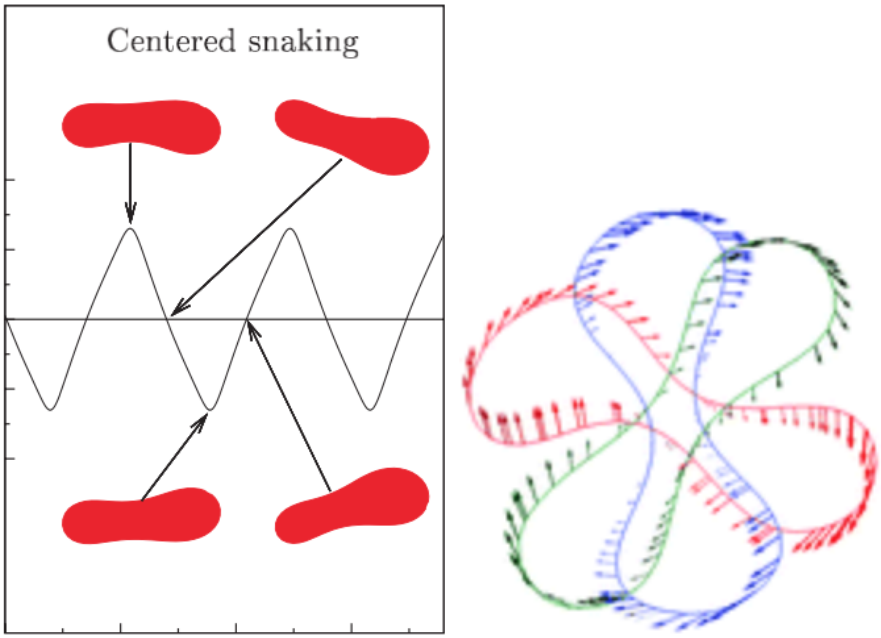

Figure 10: Schematic showing snaking (left)[27] and tumbling (right)[28]

2.2.1 Poiseuille Flow

In the majority of human vasculature (that is to say anywhere that isn't the heart, the major vessels connected to the heart, an aneurysm or the capillaries which have a radius comparable to that of an RBC) blood has the flow profile associated with a shear thinning fluid in a laminar regime. Before we discuss shear thinning fluids, we will consider a simpler flow profile - namely a Poiseuille flow[22]. If a Newtonian fluid is flowing in a cylindrical pipe and its viscous forces dominate its internal forces (low Reynolds number), it will have a Poiseuille flow profile. This means that the flow is fastest in the center of the tube and slowest near the walls. This creates a parabolic flow profile with increasing shear rate from the centre to the wall. The equations describing a Poiseuille flow are as follows[22]. We begin by considering a pipe with a radius R and length l. The pressure gradient across the pipe is given by $\frac{dp}{dx}$ and the axial flow velocity at a given radial point in the flow is $u_x(r)$. Now let's consider the fact that the fluid is incompressible and thus

$$\frac{\partial u_x}{\partial x} = 0 \tag{1}$$

Further assuming that the flow is axisymmetric and has uniform viscosity, the Navier-Stokes equations reduce to

$$\frac{\partial p}{\partial x} = \mu \left(\frac{\partial^2 u_x}{\partial r^2} + \frac{1}{r} \frac{\partial u_x}{\partial r} \right) \tag{2}$$

$$\frac{\partial p}{\partial r} = 0 \tag{3}$$

Then using separation of variables and integrating twice with respect to r, we get

$$u_x(r) = \frac{r^2}{4\mu} \left(\frac{dp}{dx} \right) + C_1 \ln R + C_2 \tag{4}$$

we now apply boundary conditions to find the integration constants. Starting with the fact that the flow velocity cannot be infinite, we can conclude that

$$C_1 = 0$$

then applying the non-slip condition (meaning that the velocity at the wall is 0) we find

$$C_2 = \frac{R^2}{4\mu} \left(\frac{dp}{dx} \right)$$

thus we have an equation for flow velocity in a Pousieulle flow

$$u_x = \frac{1}{4\mu} \left(-\frac{dp}{dx} \right) (R^2 - r^2) \tag{5}$$

Equation 5 clearly shows that the velocity will be highest in the centre of the vessel (r=0). We can then integrate this expression over area in order to give the volumetric flow rate

$$\dot{Q} = \int_0^R 2\pi r u_x dr = \frac{\pi R^4}{8\mu} \left(-\frac{dp}{dx} \right) \tag{6}$$

Finally the shear stress at a given point in the flow may be given by

$$\sigma_{rr} = -\frac{r\Delta p}{2l} \tag{7}$$

where σ_{rr} is the shear stress at a given point (polar coordinates), Δp is the pressure drop in the pipe. Equation 7 clearly shows that the shear stress will have a maximum value at the vessel wall (maximum radius).

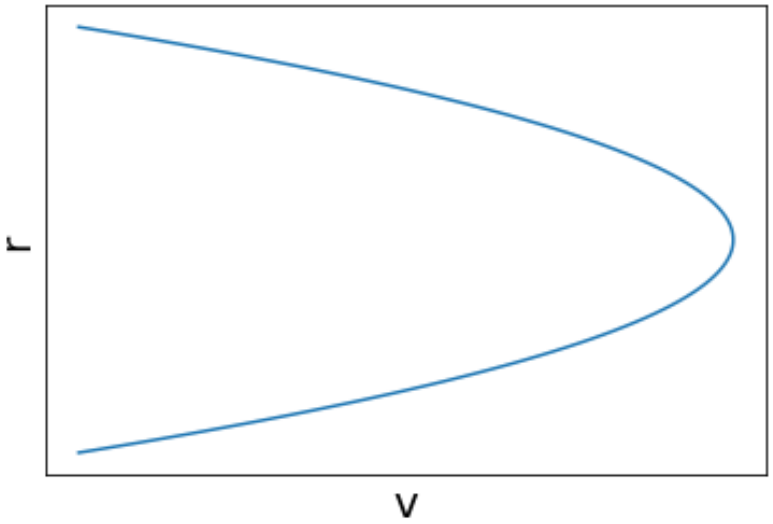

Figure 11: Axial flow velocity against radial position for a Poiseuille Flow

Earlier in the chapter we talked about how healthy RBCs tend to either parachute or slipper. We also talked about the fact that parachuting tends to happen closer to the centre and slippering tends to happen closer to the vessel walls. If one were to picture a red blood cell close to the centre it is easy to reason that the outside rim of the RBC will be folded backwards due to the differential shear stresses on each side of the centre. This of course will not be the case close to the wall and thus slippering is more likely. It has also been observed that parachuting is more likely to occur in a small vessel, whereas slippering is more likely to occur in a large vessel. We can quantify this using confinement, which is the ratio between RBC radius and vessel radius. At high confinement ratios parachuting is more likely, because of the steeper shear gradients which are able to fully deform the RBC[13]. The slipper and parachute shapes are stable, because they impede the background fluid less than biconcave disc shaped RBCs[14].

2.2.2 Shear-Thinning Fluids

Blood is a non-Newtonian fluid, because its viscosity varies under shear. Specifically blood is a shear thinning fluid, meaning that its viscosity reduces under shear. This is due to the fact that RBCs tend to aggregate when subjected to low local shear forces and spread when subjected to high local shear forces. This in turn reduces local viscosity[15].

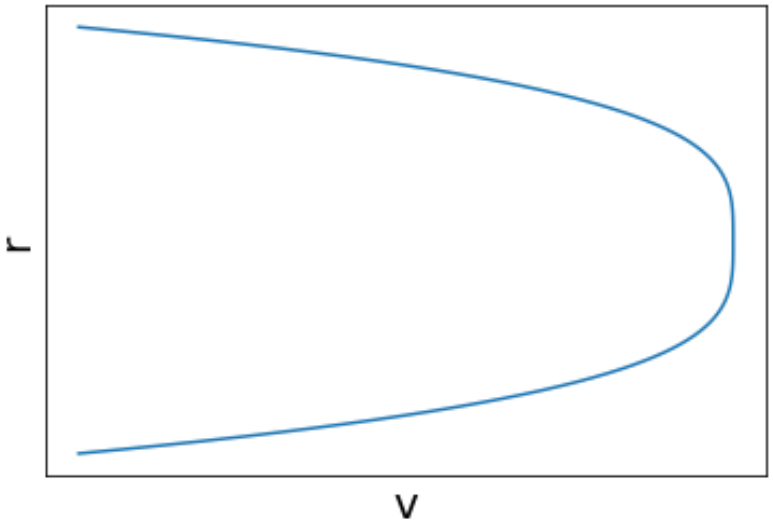

Figure 12: Axial Flow velocity against radial position for a shear thinning fluid

As can be seen in figure 12 the front of the flow profile for a shear thinning fluid is truncated relative to a Newtonian fluid in a Poiseuille flow. This is the characteristic flow profile that we expect to see in blood flow.

The profile in figure 12 was produced using the power law fluid equation. This is an equation which relates shear stress to shear rate and from which a one dimensional velocity profile can be derived. The power law fluid equation is as follows.

$$\tau = K\dot{\gamma}^n \tag{8}$$

where τ is the shear stress, K is the Flow Consistency index, $\dot{\gamma}$ is the shear rate and n is the flow behaviour index. $n = 0$ for a Newtonian fluid, $n < 1$ for a shear thinning fluid and $n > 1$ for a shear thickening fluid.

By rewriting this in a differential form we can derive an equation for a one dimensional velocity profile

$$\tau = K\left(\frac{\partial u}{\partial r}\right)^n \tag{9}$$

then introducing the axial momentum equation

$$\frac{-dp}{dx} + \frac{1}{r}\frac{\partial(r\sigma_{xr})}{\partial r} = 0 \tag{10}$$

therefore

$$\frac{\partial(r\sigma_{zr})}{\partial r} = \frac{rdp}{dx} \tag{11}$$

$$\int \frac{\partial(r\sigma_{xr})}{\partial r}dr = \int \frac{rdp}{dx}dr \tag{12}$$

therefore

$$r\sigma_{zr} = \frac{r^2}{2}\frac{dp}{dx} \tag{13}$$

Then approximating the pressure gradient as the pressure drop over the vessel length we get

$$\frac{dp}{dx} \approx \frac{\Delta p}{l} \tag{14}$$

$$r\sigma_{zr} = \frac{r^2}{2}\frac{\Delta p}{l} \tag{15}$$

$$\tau = \frac{r\Delta p}{2l} \tag{16}$$

then using the equation for wall shear stress

$$\sigma_{wall} = \frac{\Delta pR}{2l} \tag{17}$$

therefore

$$\tau = \frac{r}{R}\sigma_{wall} \tag{18}$$

$$\frac{r}{R}\sigma_{wall} = K\left(\frac{\partial u}{\partial r}\right)^n \tag{19}$$

therefore

$$\frac{\partial u}{\partial r} = \left(\frac{r}{KR}\sigma_{wall}\right)^{\frac{1}{n}} \tag{20}$$

integrating both sides with respect to r we get

$$\int_r^R \left(\frac{\partial u}{\partial r}\right)dr = \int_r^R \left(\frac{r}{KR}\sigma_{wall}\right)^{\frac{1}{r}} \tag{21}$$

$$u = \left[\left(\frac{\sigma_{wall}}{KR}\right)^{\frac{1}{n}} \frac{r^{\frac{1}{n}+1}}{\frac{1}{n}+1}\right]_r^R \tag{22}$$

applying limits we end up with

$$u = \left(\frac{\sigma_{wall}}{KR}\right)^{\frac{1}{n}} \frac{R^{\frac{1}{n}+1} - r^{\frac{1}{n}+1}}{\frac{1}{n}+1} \tag{23}$$

It is now worth talking about the non-dimensional numbers which are important in blood flow. There are two key numbers to consider. The first is called the Capillary number[16]. This is a ratio of the viscous forces to the stiffness forces and it is important because, a change in Capillary number will significantly alter flow dynamics and as such when we are simulating blood flow, we can say that two experiments with the same Capillary number are similar and easy to compare. The Capillary number is given by

$$Ca = \frac{\mu \dot{\gamma} r_{RBC}}{k_s} \tag{24}$$

where μ is the dynamic viscosity, $\dot{\gamma}$ is the shear rate and k_s is the shear stiffness of the RBCs. The other key dimensionless number is the Föppl–von Kármán number[17]. This is the ratio between shear stiffness and bending stiffness. This is very important for two reasons. The first is that RBC stiffness varies in Sickle Cell Disease and the second is that in order to set up realistic simulations we must choose shear and bending stiffness values which are in the correct proportion to each other. The Föppl–von Kármán number is given by

$$\Gamma = \frac{k_B}{r_{RBC}^2 k_s} \tag{25}$$

where k_B is the bending stiffness of the cell.

2.3 Einstein Viscosity

Fluids with low volume fraction particle suspensions $\phi < 0.03$ can be modelled as Newtonian Fluids with an effective viscosity. Derived by Einstein in 1906[8], the formula for calculating this effective viscosity is as follows

$$\eta = \eta_0 \left[1 + \frac{5}{2}\phi\right] \tag{26}$$

where η is the effective viscosity, η_0 is the viscosity of the background fluid and ϕ is the volume fraction.

It works on the assumption that if the particles are rigid spheres, they will resist the shear stress imposed on them by the flow. This in turn generates a viscosity term in addition to that of the standard fluid viscosity. Other important assumptions include the small size of the particles relative to the volume of the fluid (ideally an infinite ratio), the distance between the particles should be much larger than the radius of the particles, and the size of the particles should be much smaller than the distance over which the shear rate varies.

We first consider the stress given by the Einstein relation in a pure simple shear flow. To understand where this relation comes from we shall consider the fact that we are in a Stokes flow regime and as such flow solutions can be superimposed. We first introduce an equation for the viscosity in a suspension flow.

$$\eta = \eta_0 + \eta_p \tag{27}$$

where η_p is the viscosity contribution of the suspended particles.

Now we shall introduce an equation for the total shear stress in the suspension

$$\sigma_{tot} = \eta_0 \dot{\gamma} + \frac{5}{2}\eta_0 \phi \dot{\gamma} \tag{28}$$

where $\dot{\gamma}$ is the shear rate. The factor of $\frac{5}{2}$ comes from Einstein's derivation [8]. Re-writing the shear stress equation as a sum over all of the suspended particles we get

$$\sigma_{tot} = \eta_0 \dot{\gamma} + \frac{5}{2}\eta_0 \Sigma_{i=1}^{N_p} \phi_p \dot{\gamma}_p \tag{29}$$

Here ϕ_p denotes the volume fraction contribution from a single particle i, and $\dot{\gamma}_p$ denotes the shear rate felt by particle i. In a Couette flow the shear rate is the same everywhere and as such the equation reduces to the Einstein viscosity equation

$$\eta = \eta_0 \left[1 + \frac{5}{2}\phi\right] \tag{30}$$

In a flow where shear rate is not the same everywhere such as the Poiseuille flows which we will be considering, we return to equation (29) but now evaluate the shear rate for each particle separately. The solvent viscosity responds to the mean shear rate, so we obtain

$$\sigma_{tot} = \eta_0 \bar{\dot{\gamma}} + \frac{5}{2}\eta_0 \Sigma_{i=1}^{N_p} \phi_p \dot{\gamma}_p(r_i) \tag{31}$$

Then dividing through by the mean shear rate we get

$$\eta = \eta_0 \left[1 + \frac{5}{2}\sum\nolimits_{i=1}^{N_p} \frac{\phi_p \dot{\gamma}_p(r_i)}{\bar{\dot{\gamma}}}\right] \tag{32}$$

This is an adapted Einstein Viscosity model which we shall use for Poiseuille flows. It is functionally equivalent to an equation derived by Howard Brenner[24].

3 Methods

For all simulations we shall be using the numerical code BioFM[25]. This code simulates blood flow, resolved at the cellular scale. The background fluid is Newtonian and there are flexible two dimensional membranes suspended in said fluid which represent RBCs. The properties of individual RBCs (stiffness, shape and size) can be changed. It is important to ensure that all simulations are physiologically realistic and numerically stable. As such we outline a method below for correctly converting between physical units and computational units, such that simulations can be set up appropriately.

3.1 Converting Between Simulation and Dimensional Units

All numerical outputs from BioFM simulations are in dimensionless units and must be converted to dimensional units in order to be compared with experimental data. We need to understand how each of the simulation quantities were derived in order to convert them back to real quantities as well as to set the simulation parameters correctly. The spreadsheet which accompanies this document can be used to calculate various parameters needed for the simulation and for converting between simulation and real units.

3.1.1 Size Scaling

First let us consider size scaling. The radius of an individual RBC is fixed at 4μm in real units and so in order to find a scaling factor between distances in the simulation world and the real world, one must divide 4μm by the number set for the RBC radius

$$C_l = \frac{r_{RBC}}{r^*_{RBC}} = \frac{4\mu\text{m}}{r^*_{RBC}} \tag{33}$$

where r^*_{RBC} is the simulation RBC radius.

The simulation RBC radius parameter can be found in the parametersMeshes.xml file and is called radius. C_l can then be used to find the dimensions of the pipe/duct. Note that one must subtract 2 from the number of mesh units in the y/z directions before multiplying by the scaling factor, because of the extra lattice point outside of the domain on each side

$$R = (N_m - 2)C_l \tag{34}$$

where N_m is the number of mesh units.

In order to find the necessary mesh fineness for a given RBC radius, a simple formula can be used

$$N_E = r^{*^2}_{RBC} \times 20 \tag{35}$$

where N_E is the number of mesh elements and the factor of 20 is there for numerical convenience. The appropriate mesh file can then be used from the BioFM code repository. It will be of the form $rbc - ico - N_E.msh$. The author of BioFM discusses mesh refinement and mesh resolution testing in [26].

3.1.2 Time Scaling

The next step is to look at time scaling. To begin with we shall establish a similar relationship to that used for size scaling

$$\Delta t = \Delta t^* C_t \tag{36}$$

where C_t is the time scaling coefficient and Δt is the imposed dimensional timestep. The dimensionless time step is equal to 1 in the code and so the dimensional time step and the coefficient are simply equal to each other and as such we can impose the dimensional timestep by choosing C_t.

Once we have imposed a time step we can use this to calculate various parameters. We begin by defining a relationship between the dimensional and dimensionless shear rate

$$\dot{\gamma} = \dot{\gamma}^* C_{\dot{\gamma}} \tag{37}$$

then using the relation

$$C_t = \frac{1}{C_{\dot{\gamma}}} \tag{38}$$

and the fact that the dimensionless timestep is always equal to 1, we can conclude that

$$\Delta t = C_t = \frac{\dot{\gamma}^*}{\dot{\gamma}} \tag{39}$$

We will see why it is convenient to derive the above ratio in the next section.

3.1.3 Stiffness Scaling

In order to ensure similarity between the simulation world and the real world we use the capillary number which is the ratio of viscous forces to internal forces

$$Ca = \frac{\mu \dot{\gamma} r_{RBC}}{k_s} \tag{40}$$

where μ is the dynamic viscosity, $\dot{\gamma}$ is the shear rate and k_s is the shear stiffness of the RBCs. The above form of capillary number is a real world form and so it represents the experiments. This capillary number must be equated to a simulation version. The asterisks represent non dimensional quantities.

$$Ca = \frac{\mu^* \dot{\gamma}^* r^*_{RBC}}{k^*_s} \tag{41}$$

The real world and simulation capillary numbers must be the same, such that

$$\frac{\mu \dot{\gamma} r_{RBC}}{k_s} = \frac{\mu^* \dot{\gamma}^* r^*_{RBC}}{k^*_s} \tag{42}$$

The non dimensional dynamic viscosity can be calculated as follows

$$\mu^* = \frac{\tau^* - 0.5}{3} \rho^* \tag{43}$$

where τ^* is the relaxation time and can be set in the file parameters.xml. ρ^* can be taken to be 1.

Next we shall define a conversion factor between the non-dimensional and dimensional shear stiffness

$$C_k = \frac{k_s}{k_s^*} \tag{44}$$

This quantity can then be calculated as follows using (42)

$$C_k = \frac{C_l \mu}{C_t \mu^*} \tag{45}$$

k_s can be taken as 5×10^{-6}N/m (for healthy RBCs) and μ can be taken as 1×10^{-3}kg/ms. Using the value we have just calculated for k_s^* we can calculate a value for the dimensionless bending stiffness using the Föppl–von Kármán number

$$\frac{k_B^*}{r_{RBC}^{*2} k_s^*} = \frac{1}{400} \tag{46}$$

For healthy red blood cells the Föppl–von Kármán number is believed to be $\frac{1}{400}$.

One should begin by rearranging (42) and using (33) and (39) to form the right hand side of (45) and thus calculating C_k. This should then be inserted into (44) to calculate k_s^* and this value should be inserted into (46) to find a value for k_B^*

3.1.4 Pressure Gradient

If the pressure gradient of the experiment to which the simulation is being compared is provided, then it can be converted to a non-dimensional pressure gradient. This value can be set as the gravity parameter in parameters.xml.

We start with an approximation of pressure gradient

$$\frac{\partial p}{\partial x} \approx \frac{\Delta p}{L} \tag{47}$$

where Δp is the pressure drop and L is the dimensional length of the pipe. Now we need to use our previously defined stiffness conversion factor in order to find a relation between the dimensional and dimensionless pressure drop

$$\Delta p^* = \frac{\Delta p C_l}{C_k} \tag{48}$$

Finally the non-dimensional pressure gradient can be found as follows

$$\frac{\partial p^*}{\partial x^*} \approx \frac{\Delta p^*}{L^*} \tag{49}$$

The above equations can also be combined into a single equation which is used in the spreadsheet.

$$\frac{\partial p^*}{\partial x^*} \approx \frac{\partial p}{\partial x} \frac{C_l^2}{C_k} \tag{50}$$

Finally we can use our size and time scaling coefficients to convert dimensionless velocities to dimensional ones.

$$\vec{v} = \vec{v}^* \frac{C_l}{C_t} \tag{51}$$

3.2 Numerical Checks

In order to ensure that we can trust our simulation results and thus have set the simulation up correctly, we need to check that running the same simulation with a different timesteps produces results in close agreement. We do this by superimposing plots of dimensional fluid velocities against dimensional timesteps. Here we have an example of a simulation being run with two different timesteps. The simulation in question is based on an experiment run by our collaborators. The experiment consists of a channel with a rectangular cross section of dimensions $20 \times 15\mu$m. The pressure gradient is $129998 \times 10^5 \text{N/m}^3$ and the cell shear stiffness is 5×10^{-6}N/m. The dynamic viscosity of the background fluid is 1×10^{-3}kg/ms.

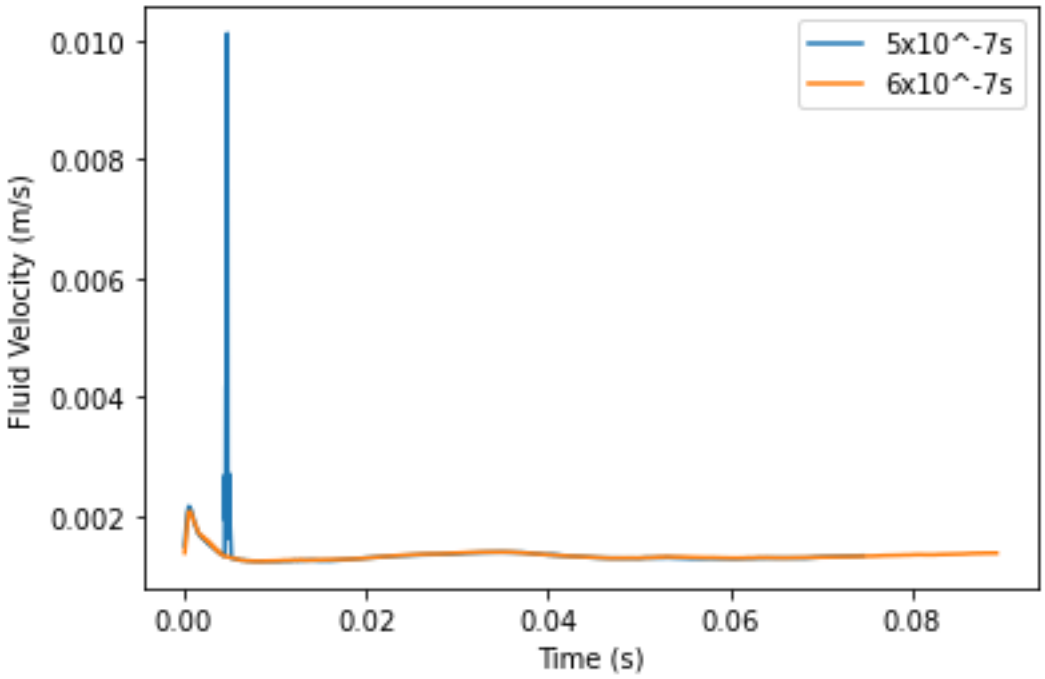

Figure 13: Two superimposed plots showing maximum fluid velocity against time. The legends indicate the respective timesteps. The parameters used in this simulation are detailed in section 1.5.

The timesteps shown in figure 13 are suitable for the simulation and as such the simulations run to completion. Below we see an example of the same simulation, but with a timestep which is too large and thus a numerical instability occurs at the time marked by the red cross. The uptick at the beginning of the simulation is simply an artifact produced when the system transitions from stationary to moving and it is not relevant as only data from the steady state is considered.

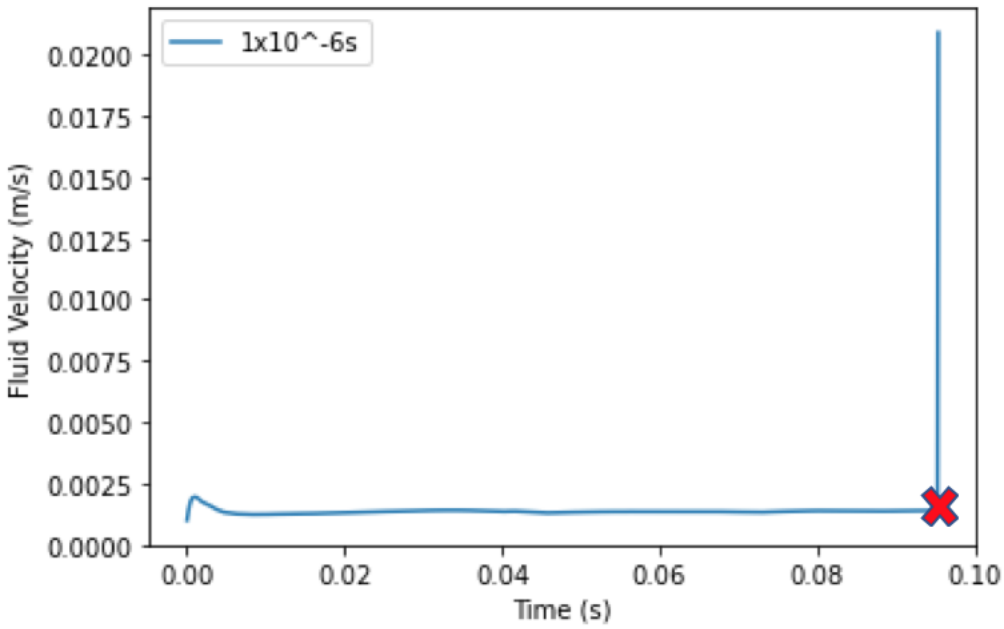

Figure 14: Plot showing maximum fluid velocity against time. The legend indicates the timestep. The parameters fused in this simulation are detailed in section 1.5. The red cross indicates that the simulation has failed at that point.

3.3 Plotting

In order to study the flow profiles produced by the simulation we need to plot the individual cell velocities in the x-direction against the position of the cell centroid along the channel width. To do this we extract the x-direction velocity and centroid position data from each cell file for a given timestep. These velocities are then converted to dimensional velocities using eq 19. It is then necessary to fit a curve to the velocity plot. To do this we shall use the Power Law Fluid, which was described in the Background section as a way to approximate a shear-thinning fluid. However in this case we shall be using a fitting equation provided by our experimental collaborators.

$$\vec{V} = \vec{V}_{max}\left(1 - \left(1 - \frac{\vec{V}_{wall}}{\vec{V}_{max}}\right)|\frac{r}{w}|^B\right) \tag{52}$$

Where w is the channel width. The parameters to be fitted are V_{max}, V_{wall} and the bluntness index B. The fitting itself is done using a non-linear least squares function through the python package scipy. The particular function is called curve fit.

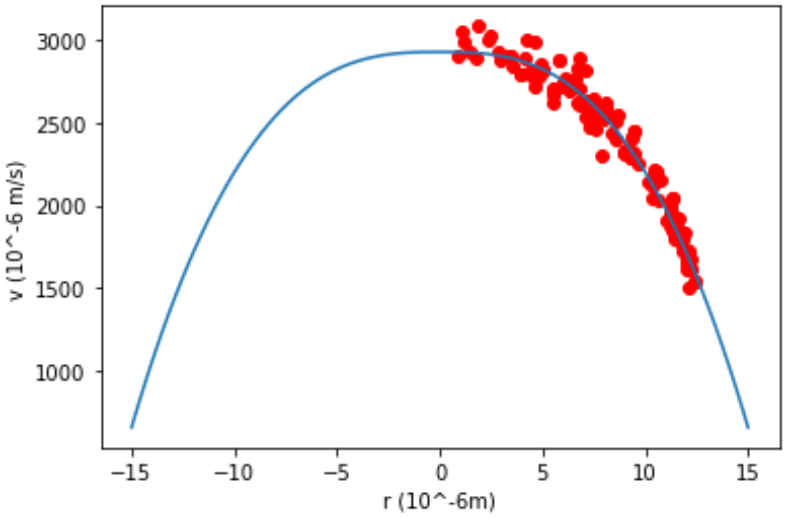

Figure 15: Plot showing velocity profile for blood flow with 30 percent Haematocrit and RBC stiffness of $5 \times 10^{-6} N/m$. The circles represent the individual RBCs and the line is the fitted curve.

Figure 15 shows an example of the plotting and curve fitting method. In this case we have healthy blood (stiffness value of $5 \times 10^{-6} N/m$. We can clearly see that the Power Law Fluid is a good fit for the data, because the circles representing the individual cell velocities all lie close to the curve.

3.4 Immersed Boundary Method

We need a method for computing the solid/fluid interactions between the RBCs and the background fluid. This method needs to calculate the forces on each RBC and the resulting deformation of the cell, as well as the individual cell velocities. The immersed boundary method (IBM) was created in order to model fluid-structure interactions for deformable bodies and is very useful for blood flow modelling and biological fluid dynamics more broadly[22]. IBM can be used with any fluid solver that supports external forcing. This means that it can be used in conjunction with Lattice-Boltzmann (the method used for updating the background fluid). All IBM calculations are performed on a Lagrangian mesh.

3.4.1 Algorithm

The process is repeated at each time-step, such that the position at time t is used to find the velocity at time $t + \Delta t$. This velocity vector can then be used to find the new position at time $t + \Delta t$ and the process can then be repeated. Of course it is not that simple however, because we must also consider the solid/fluid interaction. At a given time t we know the positions of all of the membrane nodes. This gives us the position of the membrane in space as well as its shape. The first step is the force spreading where the fluid nodes are collecting force data. Then this force data can be used to update fluid dynamics in the Lattice-Boltzmann step. Next the velocity data from the updated fluid is collected by the membrane nodes and together with the position data is used

to find the updated membrane node velocity. This can then be used to find the new position of each membrane node, which gives us the new position of the membrane in space as well as its new shape from any deformation that might have occurred[25].

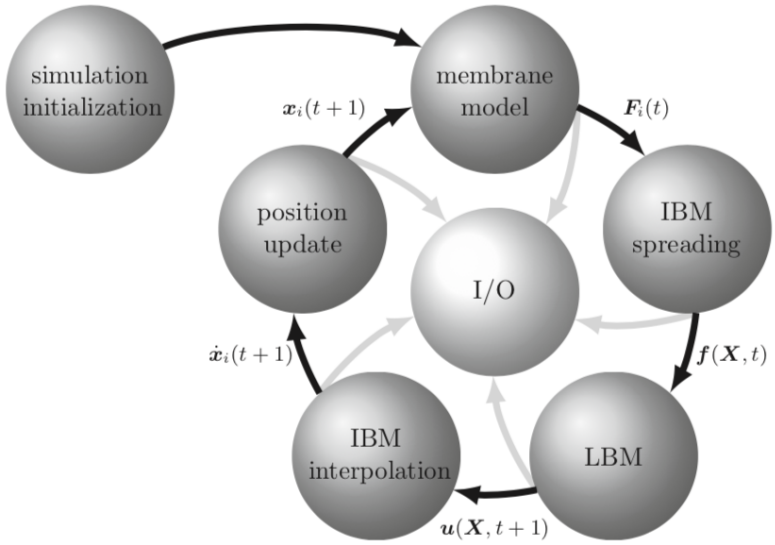

Figure 16: Schematic showing the order of steps in the BioFM code which are performed at each timestep.

3.4.2 Membrane Model

We shall now look in more detail at the membrane model itself. The membrane is a 2D surface made up of Lagrangian nodes. Three nodes are connected together to make a triangular face. The number of triangular faces defines the mesh fineness. At equilibrium the membranes have a default biconcave disc shape. The membranes in the code are designed to have a large amount of flexibility allowing them to morph into a practically infinite number of variations (provided topology is conserved). The triangular faces themselves can deform by changing the angles between edges as well as the length of the edges. They can also deform relative to each other by changing the angle between themselves and the adjacent faces[25].

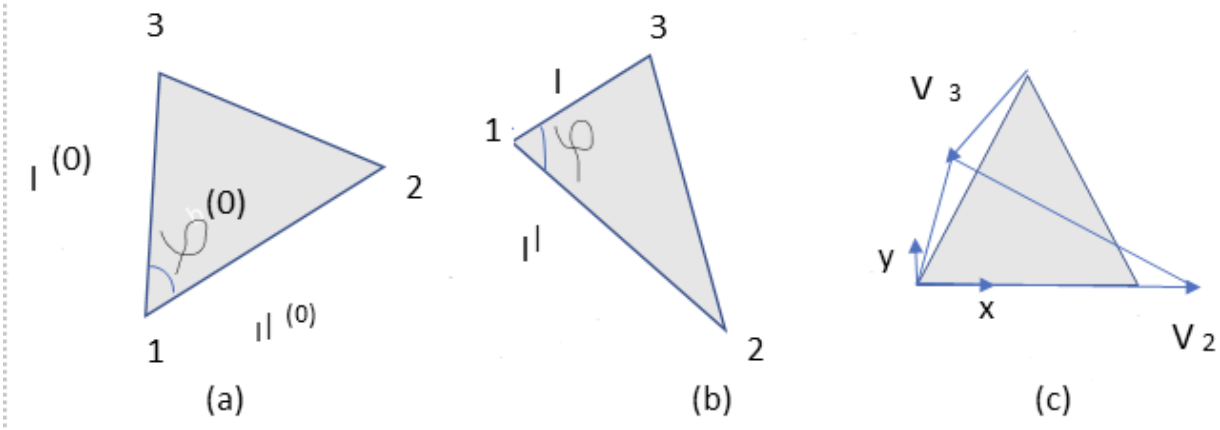

Figure 17: Schematic showing how the triangular faces can deform within themselves and relative to each other. φ is the angle between the edges and l and l' are the edge lengths on either side of the angle. Values with a 0 as an index are the original values and those without are the deformed values. V_2 and V_3 are the displacement vectors[25].

4 Dilute Flow

We have run dilute flow simulations with spherical particles as a toy model for blood flow. The key advantage of this toy model is the ability to perform analytical calculations instead of purely relying on numerical methods as we will have to for dense suspensions. Additionally we will be able to better study core mechanisms of suspension mechanics which will be cleaner than in more dense suspensions. This in turn will allow us to gain insight into the effects of increasing volume fraction and increasing particle stiffness. The effects of particle shape will not be studied here. As previously stated, the term dilute in this case refers to volume fractions smaller than three percent.

The set up of our experiment is as follows. We have a rigid tube with a circular cross section. The tube has a radius of 15μm and a length of 64μm. The radius of each individual is 4μm. Periodic boundary conditions are used, such that a when a particle exits one end of the tube, it re-enters the other end with the correct orientation. The background fluid has the same viscosity as water ($1 \times 10^{-3} Pas$). Computations will be performed with BioFM, using the method of setting up the simulation detailed in the methods chapter. Data extraction analysis is also detailed in the methods section. Analyses of the experiments shall be done using our modified Einstein Viscosity model, as well as the original Einstein viscosity model for comparison. As a reminder, our adapted Einstein model is as follows

$$\eta = \eta_0 \left[1 + \frac{5}{2} \Sigma_{i=1}^{N_p} \frac{\phi_p \dot{\gamma}_p(r_i)}{\bar{\dot{\gamma}}} \right] \tag{53}$$

where η is the effective viscosity, η is the viscosity of the background fluid, ϕ_p is the volume fraction of an individual particle and $\dot{\gamma}_p(r_i)$ is the shear rate on an individual particle (based on its radial position).

To begin with we shall look at stiff spherical particles. It is worth noting that Einstein Viscosity was derived with the assumption of infinitely rigid spheres and so this may be a source of error. We shall at first study the effect of increasing volume fraction (but keeping stiffness the same). We begin with one particle and increase the number until we have six particles (this takes slightly above the dilute limit in this system).

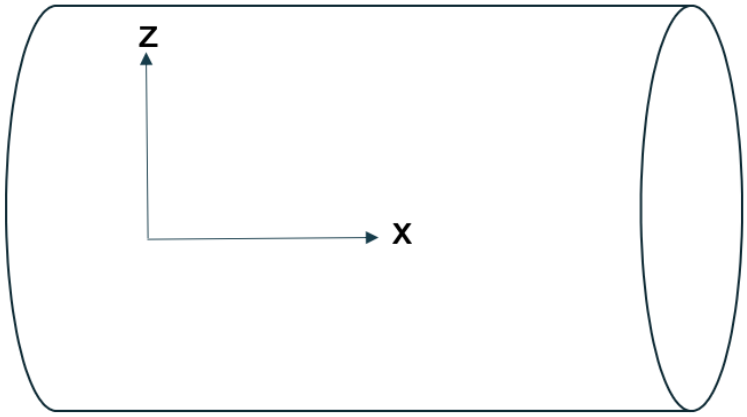

Figure 18: Schematic of the dilute flow simulation set up.

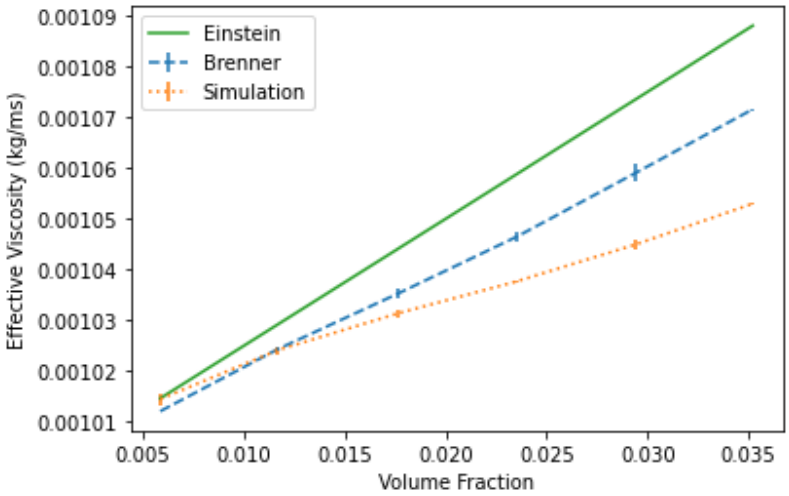

Figure 19: Plot of volume fraction against effective viscosity for dilute suspensions, with sphere shear stiffness of $5 \times 10^{-5} N/m$. Background fluid viscosity is $1 \times 10^{-3} kg/ms$. Values from the simulation output are compared against our adapted Einstein Viscosity model (labelled Theory) and the original Einstein Viscosity model (labelled Einstein).

Figure 19 shows some promising results in a number of key ways. First, all three plots are roughly linear. This is to be expected at very dilute suspension concentrations and agrees well with Einstein's theory. Second all of these plots will intercept the y- axis (if extended) at approximately the correct value; namely the viscosity of the background fluid $1 \times 10^{-3} kg/ms$. This shows that the simulation has been set up correctly. Thirdly, both analytic models give values close to that of

the simulation output. Finally, our adapted Einstein Model is closer than the traditional Einstein Model. It is worth noting that many of the error bars which appear in this section are too small to be seen. This is simply because the standard error for those results is very small relative to the y-axis scale.

The simulation output gives the lowest value of effective viscosity, followed by our adapted model and then the traditional Einstein Viscosity model. This is reasonable for the aforementioned reason that Einstein viscosity (and by extension our adapted model) assumes infinitely rigid spheres and our spheres have some level of flexibility. For this reason we can expect a lower level of effective viscosity from our simulation output. The reason that our adapted model predicts a lower effective viscosity than traditional Einstein is due to the fact that we are accounting for different shear rates on different spheres (depending on their position in the flow). Finally it is worth mentioning that at very low volume fractions, the three plots are effectively equal. This shows that Einstein Viscosity is highly accurate at very low volume fractions. This is not unexpected, for two reasons. The first is that the error incurred by one or two spheres is smaller than that incurred by a greater number of spheres. This is a simple statistical effect. Secondly the fluid volumes in all of the simulations are the same and considering that an aforementioned assumption of Einstein viscosity is that the ratio between the sphere radius and the pipe radius is ideally infinite, we can expect better results in the more dilute cases.

Now we shall look at the effect of particle stiffness on effective viscosity. This is important in the broader context of Sickle Cell Disease, where cell stiffness is extremely important. As such we shall run simulations with a single sphere of increasing stiffness.

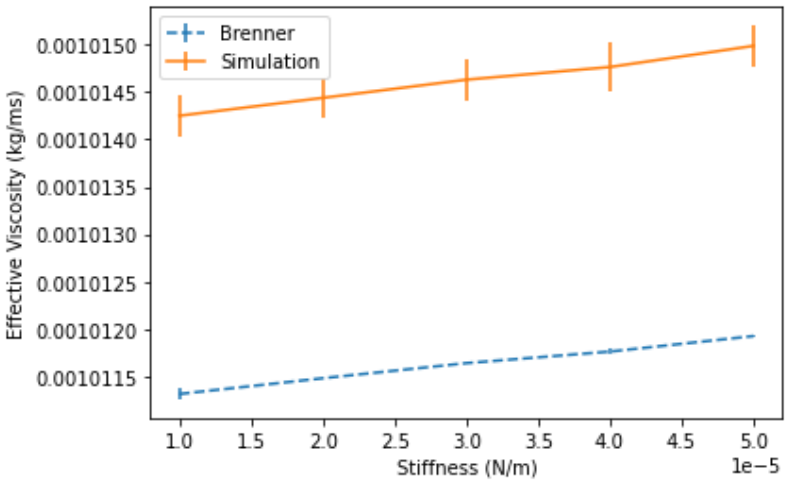

Figure 20: Plot of stiffness vs effective viscosity for a single sphere. The simulation output is compared to our adapted Einstein model.

Figure 20 shows how effective viscosity increases with an increase in sphere stiffness (we can see a plot with a positive gradient). This is to be expected, because it is harder for a fluid to move past

a sphere when it is less able to deform it. The relationship between stiffness and effective viscosity appears to be approximately linear. This is because there is a linear inverse relationship between fluid velocity and viscosity, meaning that if the fluid velocity decreases approximately linearly as stiffness is increased, then we expect a linear relationship between stiffness and viscosity. A similar argument can be made for radial position in our adapted model. Of course the traditional Einstein model is of no use in this experiment, because it depends purely on volume fraction and does not take stiffness into account. Given that our model accounts for position, which in turn accounts for stiffness (as explained in the background chapter), it is of use in analysing this experiment. The plots based on theory and simulation follow each other exactly, which shows the direct link between sphere radial position and fluid velocity. It must be noted that while there is a clear trend, the absolute difference in effective viscosity as stiffness ia increased is very small. This means that stiffness does not have an enormous effect when only one sphere is considered.

Finally we shall take a deeper look at how radial position changes with stiffness and what effect this has on effective viscosity.

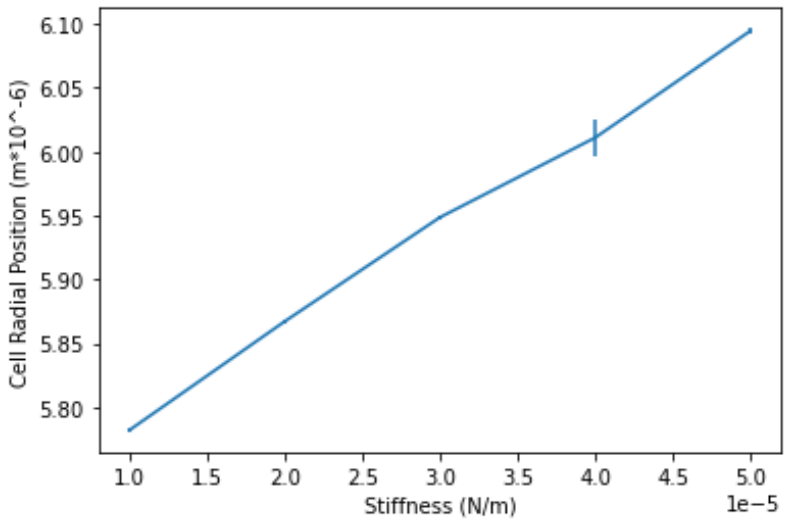

Figure 21: Plot of stiffness vs radial position for a single sphere.

In figure 21 we can see this approximately linear relationship between stiffness and the radial position of the sphere. In the background chapter we discussed how a less rigid particles experiences a greater lifting force from the vessel wall and as such moves closer to the centre of the vessel (smaller radial position). This in turn subjects the sphere to a greater shear stress and as such increases its contribution to effective viscosity. The positive correlation is therefore expected, but what is interesting is the approximately linear nature of the relationship. This would explain why we see an approximately relationship for the theoretical model in figure 4. It also gives an indication as to how well behaved and predictable such a dilute suspension flow is.

We shall now compare this to a fluid velocity plot.

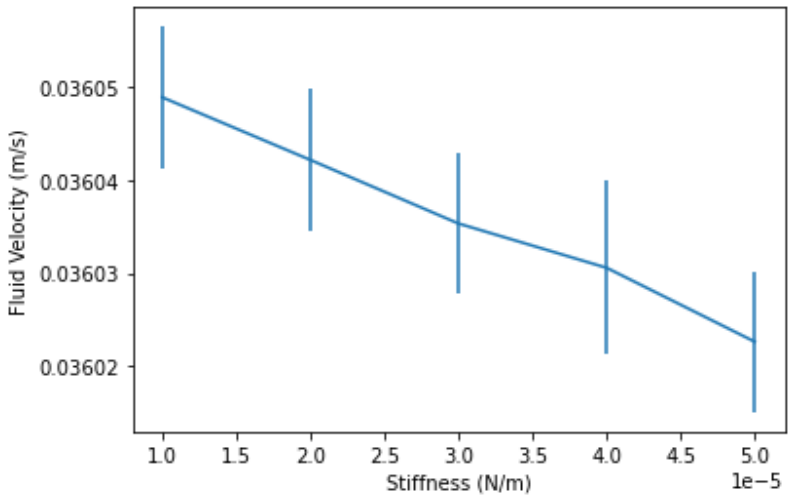

Figure 22: Plot of stiffness vs fluid velocity for a single sphere.

In figure 22 we can clearly see why the two plots in figure 19 follow the same trajectory. The flow velocity mirrors the radial position plot. Not only does this explain figure 19, but it also gives us a very interesting fluid dynamics result. We can see a similar and opposite effect on both radial position and fluid velocity from an increase in stiffness. It is not clear if it is the radial position or the lack of compliance which is the dominant effect as it is impossible to isolate them. Likely both of these effects are working in conjunction.

From these results we have learned the following things. First we have clearly seen Einstein's theory of viscosity give results close to those given by the simulation output, both in terms of the linearity of the volume fraction vs viscosity plot and in terms of the specific values in these plots. Our adapted Einstein Model outperforms the traditional Einstein Viscosity model in that it achieves results closer to the simulation results. This is due to the fact that we are accounting for the shear stress on each particle based on their radial positions. We have also shown that our adapted Einstein model can account for changes in particle stiffness. This is again because we account for the radial position of the particles which move closer to the vessel wall when they are stiffer (smaller lifting force) and thus experience a larger shear force. Finally we have shown the direct correlation between sphere stiffness, radial position and effective viscosity. This has been shown by the the fact that the stiffness vs radial position plot and the stiffness vs fluid velocity plot mirror each other.

5 SCD Blood Flow

We shall now study the effect of heterogeneity in SCD on blood flow rheology, considering the effects of both cell stiffness and shape. Unlike the dilute suspension flows in the previous chapter, these simulations involve dense suspensions and as such must be analysed numerically. Starting with healthy blood and then looking at SCD blood, we shall extract velocity profiles as well as mean

fluid velocities from the simulations, so that we can compare different RBC property distributions (both homogeneous and heterogeneous). This means that we will be able to study the effects of RBC properties (stiffness and shape) on blood flow rheology as well as the effects of heterogeneity.

The simulations have a realistic Haematocrit of 30 percent. This is a reasonable Haematocrit for a healthy adult without Anemia. The set up for the experiments is as follows. We use a rigid pipe with a circular cross section. The pipe has a radius of $15\mu m$ and a length of 64μm. A pressure gradient of $1.3 \times 10^5 N/m^3$ is used (based on a setup used by our experimental collaborators). A mixture of biconcave disc shaped cells and spherical cells. The spherical cells are an approximation of a type of sickled cell which takes the form of a spiky ball. The radius of the biconcave RBCs is 4μm and the spherical cells have been volume matched, such that their radii are $2.895\mu m$. Periodic boundary conditions are used, such that a cell which leaves one end of the pipe will enter from the other end with the correct orientation. The background fluid is Newtonian and has the viscosity of water. Computations will be performed with BioFM, using the method of setting up the simulation detailed in the methods chapter. Data extraction analysis is also detailed in the Methods section.

To begin with we shall look at healthy blood. That is to say RBCs with a stiffness of 5×10^{-6}N/m. All RBCs in this simulation start with a biconcave disc shape. This is a good starting point, because healthy blood flow is better understood than SCD blood flow and so we can check if the simulations are working as expected and have been set up correctly. It also gives us a baseline against which to compare the simulations with SCD blood.

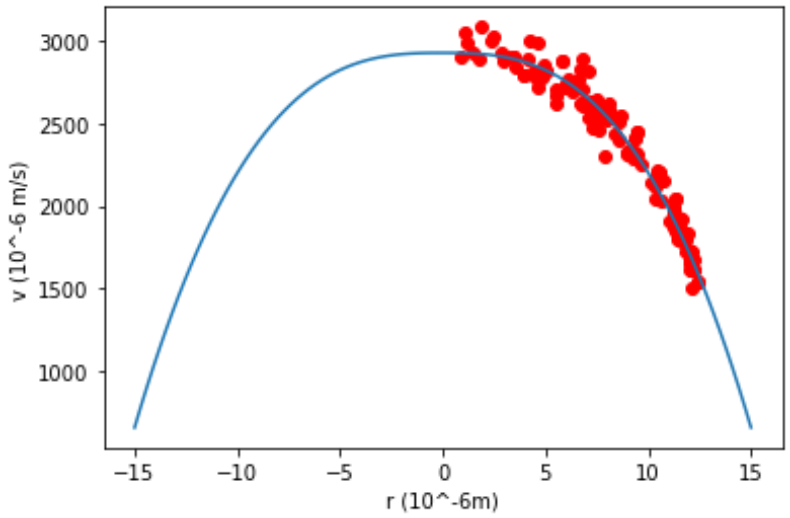

Figure 23: Plot showing velocity profile for blood flow with 30 percent Haematocrit and RBC stiffness of $5 \times 10^{-6} N/m$. The circles represent the individual RBCs and the line is the fitted curve.

In figure 23 we can see a velocity profile for healthy blood. It is clear that the power law fluid (shown by the blue curve), approximates this velocity profile very well, because the RBCs (represented by red circles) all sit close to the curve. The power law fluid and fitting method are outlined in the Methods section The next thing to note is that we have the classic shear thinning profile,

which is to say a Poiseuille flow profile with a blunted top. From now on, when we talk about how blunt a flow profile is, we are talking about the relative width of the flat part at the top of the profile. In this case the bluntness is clearly present, but it is not very blunt for the healthy blood. The velocity of the RBCs is of a reasonable order of magnitude for RBCs in a small blood vessel, such as a capillary or minor vein. We can also see that none of the cells are at the maximum radius (wall radius), indicating that we have a cell free layer as expected. We expect a cell free layer, because cells experience a lifting force from the vessel walls and as such there will be a lubricating layer of background fluid between the outer most cells and the vessel wall. These features of the plot indicate that the simulation has been set up in a reasonable fashion and has run as expected.

Now we shall increase the stiffness of all of the RBCs whilst keeping everything else the same. We can then extract the average fluid velocity from each simulation in order to obtain a quantitative comparison. This gives us a parameter sweep for homogeneous cell property distributions. It makes sense to look at homogeneous distributions first, because they are simpler to analyse and understand than heterogeneous ones.

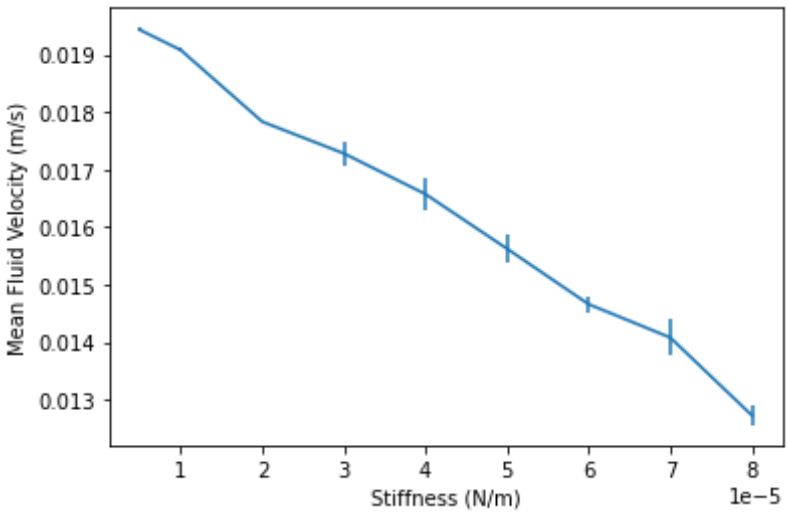

Figure 24: Plot showing RBC stiffness against mean fluid velocity. All RBCs have the same stiffness and all RBCs start with a biconcave shape.

Figure 24 shows that the mean fluid velocity decreases with an increase in cell stiffness (the line has a negative gradient). This is to be expected, because the fluid cannot move past the cells as easily if they are less compliant. Although the stiffness value for healthy RBCs is well known, it is not known how stiff sickled cells can get. Therefore the main point of the above experiment is to work out an approximate working upper bound for SCD stiffness. This is not the maximum possible stiffness, but rather a good value for us to consider for very unhealthy cells. From this experiment we have concluded that a stiffness of 8×10^{-5}N/m is a good working upper bound. This may seem like an odd conclusion if one only considers figure 2, because the graph does not seem to be tailing off. However this conclusion becomes apparent when looking at individual flow profiles.

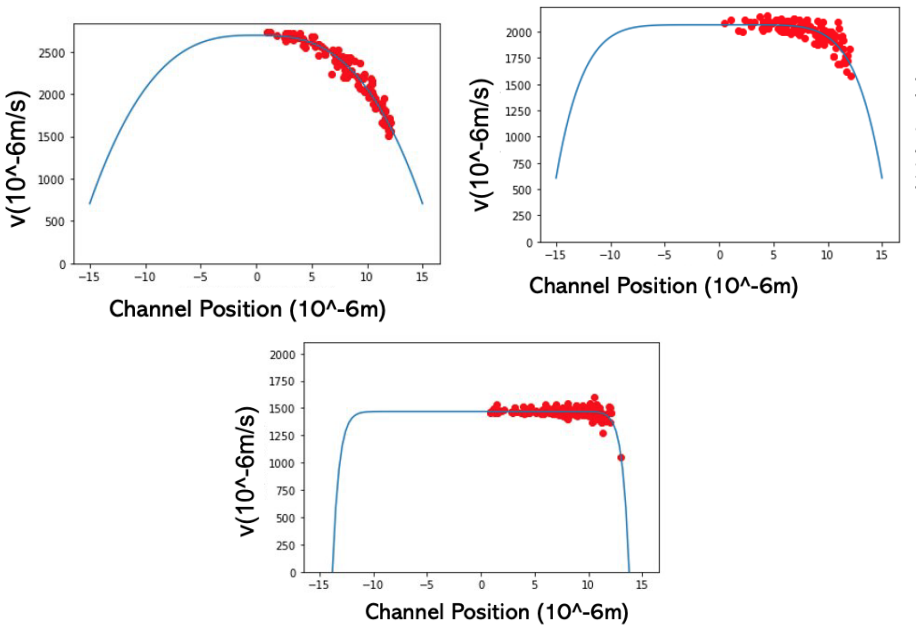

Figure 25: Plot showing velocity profiles for blood flow with 30 percent Haematocrit and RBC stiffness of 1×10^{-5}N/m, $4 \times 10^{-5} N/m$ and 8×10^{-5}N/m respectively. The circles represent the individual RBCs and the line is the fitted curve.

In figure 25 we can see how the cell velocities decrease with increasing cell stiffness. Crucially we can also see increased bluntness. Bluntness increases as the cell velocity range becomes smaller and smaller. Once all of the cells have virtually the same velocity, we have a plug flow. It can be seen that at a stiffness of $8 \times 10^{-5} N/m$ almost all of the cells have virtually the same velocity and thus we have an almost complete plug flow. This is the reason why we are considering $8 \times 10^{-5} N/m$ to be an acceptable working upper bound for very unhealthy cells. It is worth noting that the BioFM code is not sufficiently accurate to determine an actual upper bound and so the aforementioned value is just an upper bound which is suitable for our purposes. We can also conclude that as stiffness increases the RBCs move at a more uniform velocity, this is perhaps a noteworthy observation in terms of the bulk flow properties for homogeneous cell property distributions.

Now we shall move on to a heterogeneous cell distribution. In this case the variable that will be heterogeneous will be cell stiffness. We have simulated a population of healthy and unhealthy cells. The percentage of unhealthy cells increases with each simulation. All unhealthy cells have a stiffness of $7 \times 10^{-5} N/m$. Everything else is kept the same as before.

In figure 26 we can see (again as expected) that the mean fluid velocity decreases with an increase in the percentage of stiff cells. This is our first look at how heterogeneity affects blood flow rheology. That is to say that different distributions of stiffness values will lead to different blood flow rheologies and dynamics. Of course this is a fairly simple example and nothing here is unexpected. The interesting part comes when we look at individual flow profiles and try to understand

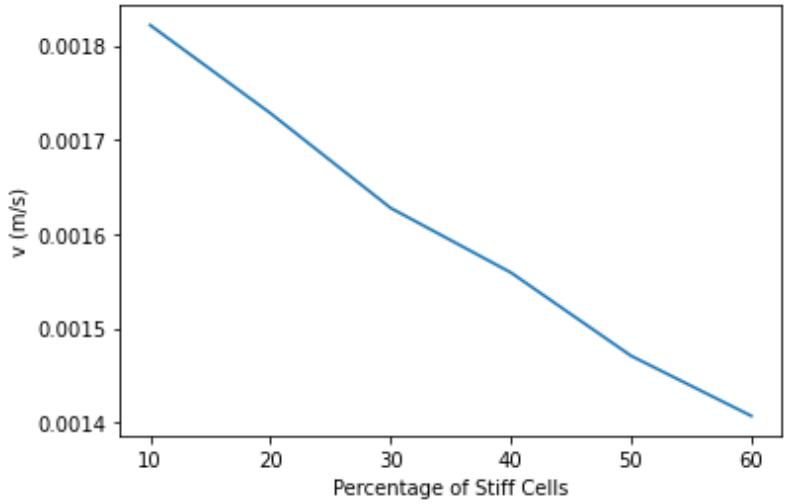

Figure 26: Plot showing percentage of stiff cells against mean fluid velocity. All RBCs have the same stiffness and all RBCs start with a biconcave shape. Healthy cells have a stiffness of $5 \times 10^{-6} N/m$ and unhealthy cells have a stiffness of 7×10^{-5}N/m

the underlying biomechanics.

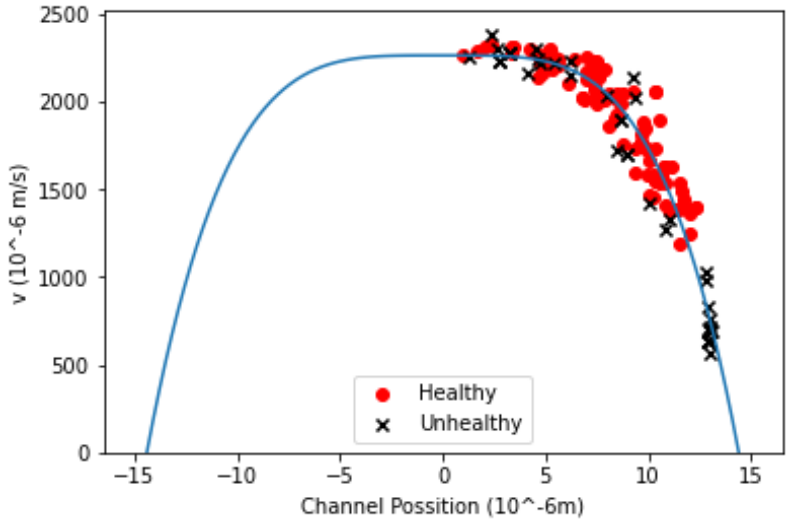

Figure 27: Plot showing velocity profile for blood flow with 30 percent Haematocrit and 30 percent unhealthy cells. The healthy cells have a stiffness of 5×10^{-6}N/m and the unhealthy cells have a stiffness of 7×10^{-5}N/m. The circles represent the individual healthy RBCs, the crosses represent the individual unhealthy cells and the line is the fitted curve.

Figure 27 shows a clear example of the margination effect. There is a cluster of unhealthy cells (indicated by the black crosses) with a lower velocity than the main bulk of the cells. These cells sit at a very high radial position with the highest shear rate and lowest fluid velocity. These stiff cells experience a smaller lifting force from the vessel walls than the healthy cells and as such migrate closer to the walls, in turn reducing the thickness of the cell free layer and thus increasing friction.

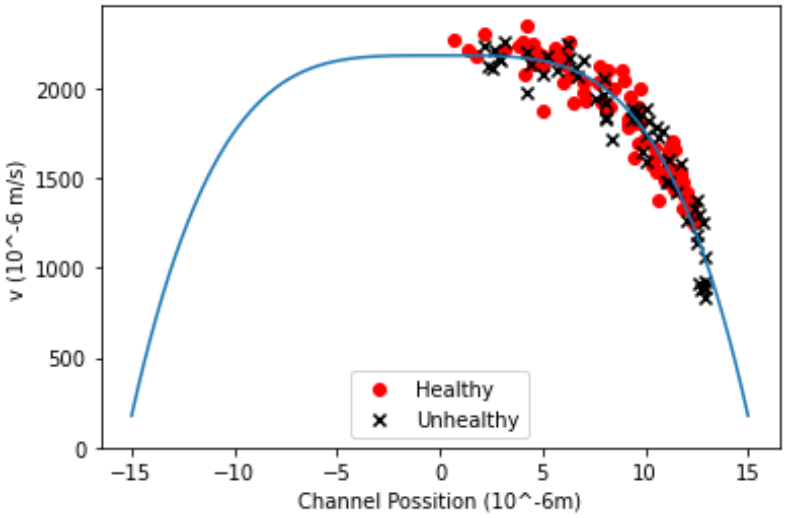

Figure 28: Plot showing velocity profile for blood flow with 30 percent Haematocrit and 40 percent unhealthy cells. The healthy cells have a stiffness of 5×10^{-6}N/m and the unhealthy cells have a stiffness of 7×10^{-5}N/m. The circles represent the individual healthy RBCs, the crosses represent the individual unhealthy cells and the line is the fitted curve.

This along with reduced cell compliance lead to the trend we see in figure 4. Now we shall compare figure 5 with a flow profile with a different percentage of unhealthy cells.

If we compare figures 27 and 28 (with figure 28 having 10 percent more unhealthy cells) we can see something quite interesting. The number of marginated cells appear to be similar in both profiles, despite the larger number of unhealthy cells in figure 28. This means that there are a larger number of unhealthy cells in the main bulk of the cells, which has in turn led to the more blunt profile which can clearly be seen in figure 28 relative to figure 27. This means that there is more uniformity in the main bulk of cells in figure 28, much like we saw in the stiffer homogeneous distributions. This is an important observation as it clearly illustrates that there are two mechanisms working in tandem. Namely the effect of margination as well as the effect of less compliant cells.

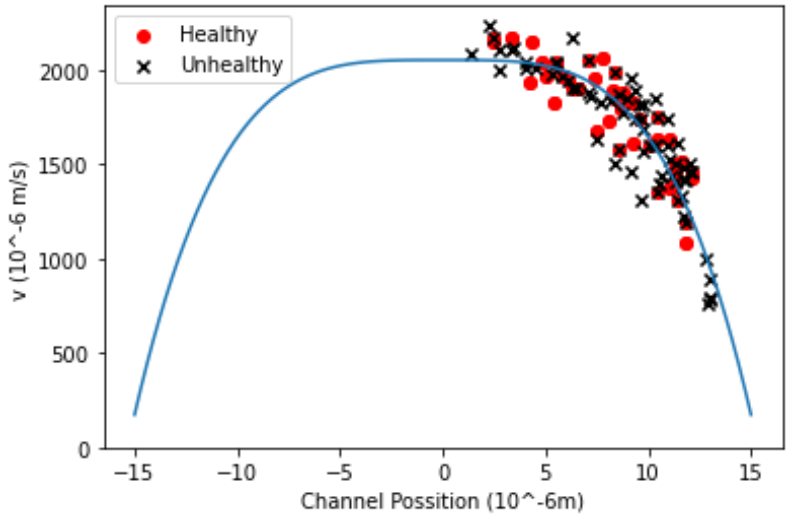

Figure 29: Plot showing velocity profile for blood flow with 30 percent Haematocrit and 50 percent unhealthy cells. The healthy cells have a stiffness of 5×10^{-6}N/m and the unhealthy cells have a stiffness of 7×10^{-5}N/m. The circles represent the individual healthy RBCs, the crosses represent the individual unhealthy cells and the line is the fitted curve.

Figure 29 reinforces the idea that the number of marginated does not really increase as the number of unhealthy cells increases. Again we have the majority of unhealthy cells joining the main bulk of cells and increasing bluntness. Again we can see the dual effects of margination and reduced compliance. This may also indicate that it is the radial position of the marginated cells that is the most important thing, rather than the number of marginated cells.

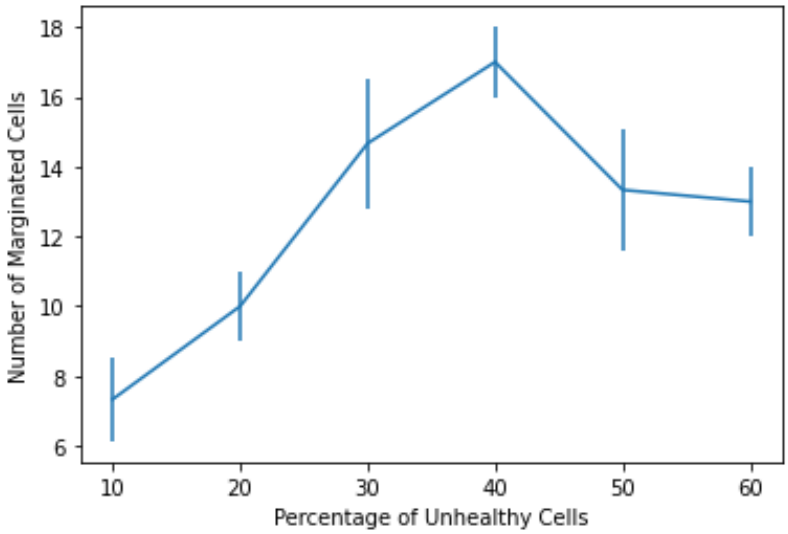

Figure 30: Plot of percentage of healthy cells vs number marginated cells. Marginated cells are defined as unhealthy cells beyond a radius of 12μm

We have now quantified the fact the number of magrinagted cells does not increase beyond 30 percent unhealthy cells. We can see this clearly in figure 29 where the graph does not increase in

height beyond an unhealthy cell percentage of 30 percent. This means that there is a point beyond which the outer part of the vessel becomes saturated (in this case we define marginated cells as those beyond a radius of 12μm) and once saturation has occurred the number of marginated cells is no longer the key issue. Instead we must look at the maximum radial position of the marginated cells.

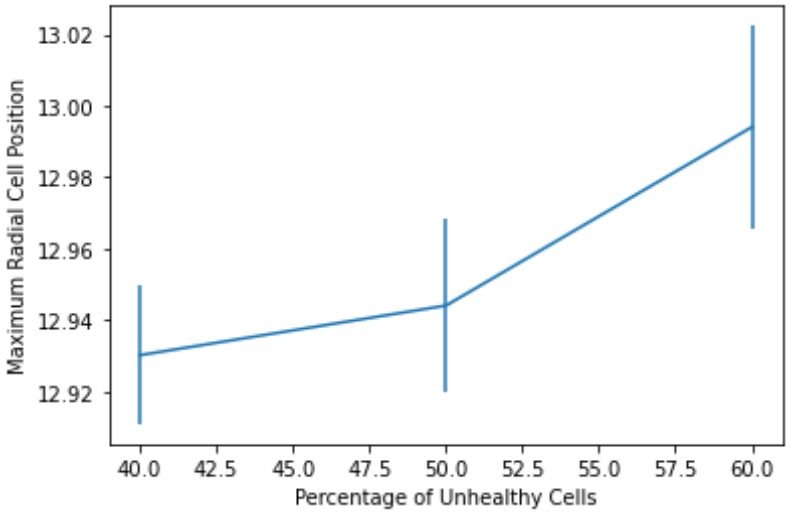

Figure 31: Plot of percentage of healthy cells vs maximum radial cell position.

It is now clear that even when the number of marginated cells stops increasing, the cells move further out and as such reduce the thickness of the cell free layer and increasing friction.

Finally we shall look at the effect of shape on blood flow rheology. For this we shall run the same experiment as that which produced figure 24, but we shall change the shapes of the cells involved. As previously mentioned, one of the common shapes which a sickled cell can take is a kind of spiky sphere. We will use spheres as an approximation for these cells. The other cells shall begin with a biconcave disc shape. In one experiment we use 100 percent biconcave discs (as before) in another experiment we use 100 percent spheres and in the third we use a 50/50 mix. Everything else is kept the same as before.

Figure 32 shows a comparison of blood flow velocity for different shape distributions, as the stiffness of the cells is increased. At lower stiffness values we can see that the spheres have the highest effective viscosity, the biconcave disc shapes have the lowest effective viscosity and the 50/50 mixture is in the middle. As we go into the plug flow regimes at the higher stiffness values, the curves cross. Understanding this phenomenon may be a key part of understanding the biomechanics of SCD.

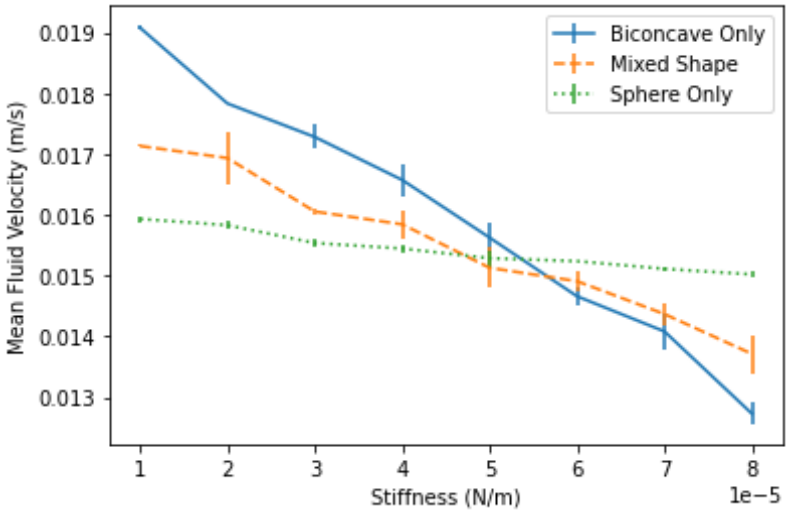

Figure 32: Plot showing RBC stiffness against mean fluid velocity. All RBCs have the same stiffness.

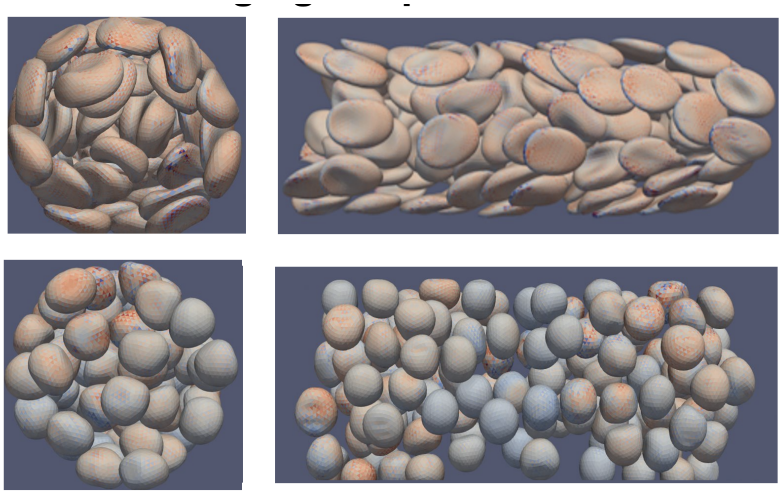

Figure 33: VTK image showing biconave disc RBCs and spherical RBCs. Cell stiffness is 1×10^{-5}N/m

At the lower stiffness values, we can understand the lower effective viscosity for RBCs compared to spheres by considering the effects of slippering and parachuting. We have observed that biconcave disc shaped RBCs have a greater tendency to form slipper shapes than spherical RBCs (as seen in figure 33). This allows them to cross fewer streamlines in the background fluid and thus move more efficiently. This has been explained in 2D. It is caused by an instability for cells in flow which are closer to a biconcave shape than a circular shape[23].

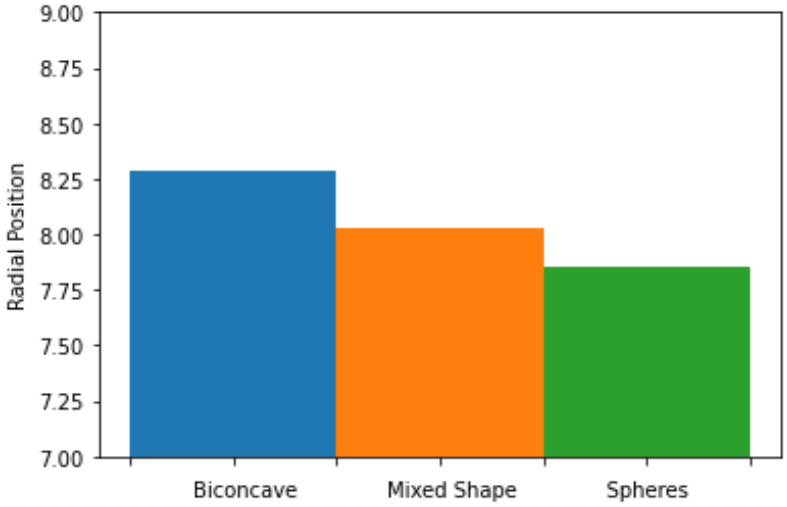

Figure 34: Plot showing mean radial positions of cells. Left: 100 percent biconcave disc, Middle: 50 percent biconave disc 50 percent sphere, Right 100 percent sphere.

The question is why does this crossover occur in the plot? To understand this we must consider the radial positions of the different shaped cells. Figure 34 shows how the mean radial cell position for our maximum cell stiffness value is greatest when 100 percent of the cells are biconcave discs and lowest when the cells are 100 percent spherical (with the mix of shapes in the middle). This tracks with the viscosity results, because it means that the thickness of the viscous free layer is smaller for biconcave disc shapes than spheres. It also means that there are a larger number of cells in the regions of higher shear rate (further increasing effective viscosity). It is not known why the biconcave discs migrate closer to the vessel wall

We have a number of key results to discuss in this chapter. First it is clear that our simulations have been set up in a reasonable manner, as evidenced by the shape of the curve and the magnitude of the RBC velocities in figure 23. Second we have shown that a plug flow forms at higher stiffness values in a homogeneous population, with an almost complete plug flow forming at 8×10^{-5}N/m (as evidenced by figure 25). This occurs as the RBCs have almost uniform velocity. Moving on to heterogeneous cell property distributions. We have seen the margination effect occurring when we have stiff cells in a population of healthy cells. The margination zone seems to become saturated when the percentage of unhealthy cells is larger than 30 percent (for this set up), however the maximum radial positions of the cells continues to increase as the percentage of unhealthy cells increases. Finally we have seen that heterogeneity in cell shape plays an important role in blood flow rheology. With biconcave disc shaped cells causing higher effective viscosity at higher cell stiffness values, with the opposite being true at low cell stiffness value (as evidenced by figure 32). This is due to the fact that the biconcave disc shaped cells deform into very efficient shapes at low stiffness values (slippers and parachutes), but migrate closer to the vessel walls than spheres at high stiffness values (as evidenced by figure 34). This implies that RBCs which retain their biconcave disc shapes may lead to more viscous blood than those which become spherical in SCD patients (at least in the more serious cases when cells become very stiff).

6 Conclusion

6.1 Conclusions

Having performed a series of computational simulations on both healthy and stiff cells, with both biconcave disc shapes and spherical shapes, in both dilute and dense suspensions, we have drawn the following conclusions. All simulations have been set up in order to ensure realistic physiology. We then extracted particle velocity and mean fluid velocity in order to produce velocity profiles and viscosity plots.

In the dilute flow regime we can draw the following conclusions. The first is that the simulations, our adapted Einstein Viscosity model and the original Einstein Viscosity model [8] all giver similar linear plots of sphere number vs effective viscosity. The second is that our adapted Einstein model is closer to the simulation outputs than the original Einstein model as we are accounting for different shear rates experienced by cells based on their radial position. Third we can see that our adapted model allows for varying stiffness and gives similar results to the simulation output for a single sphere of increasing stiffness. Fourth we can see a clear correlation between radial position and effective viscosity as well a a perfect inverse correlation between radial sphere position and mean fluid velocity. This effect is well known [17], but we have shown it independently through our simulations and analytical models.

The first conclusion we can draw about SCD flow is as follows. We have shown that sickled RBCs which retain their biconcave disc increase effective viscosity more than spherical RBCs at higher stiffness values. This is contrary to the effective viscosity of these cells at lower stiffness value. This seems to be because at lower stiffness value the biconcave disc shaped RBCs slipper and thus cross fewer streamlines than their spherical counterparts. As the particles get stiffer and move into the plug flow regime, it seems that the thickness of the cell free layer becomes important. The biconcave disc shapes are getting closer to the vessel walls than the spheres It is this reduction in the thickness of the cell free layer which seems to lead to a greater contribution from the biconcave disc shaped cells than the spherical cells.

The second conclusion we can draw is that velocity profile becomes blunter as cell stiffness is increased and cell velocity becomes more uniform. This means that the RBCs have an almost uniform velocity. We can see this effect very clearly beyond $10\times$ stiffness of a healthy cell. This gives us some insight into the mechanics of simplified homogeneous cell property distributions.

The third conclusion is that in a heterogeneous mix of cells (with healthy and unhealthy stiffness values) we see a similar number of cells being marginated, even as the percentage of unhealthy cells is increased. The main thing that changes is how far the unhealthy cells are marginated (and thus how thin the cell free layer becomes etc). In each case the majority of the unhealthy cells are in the main bulk of the cells and as such increase the bluntness of the flow profile.

6.2 Future Work

We recommend that the focus of future work should be to understand heterogeneity in SCD better, by running simulations with a larger variety of cell shapes, sizes and stiffness values. The other focus should be to include realistic vascular geometries as well as compliant vessel walls. In the short term this would help with understanding how different cell property distributions lead to different blood flow rheologies in SCD. The realistic vascular geometry would allow further study of how different cell property distributions lead to vaso-occlusion and if/where it shall occur.

In the long term this could be developed into a clinical tool which will use a combination of medical imaging and haematological tests alongside computational blood flow modelling, in order to predict if and where vaso-occluaion will occur in a specific patient. This would likely involve extending this work to the continuum scale.

Further collaboration with our experimental collaborators would also be highly recommended. The hope being that this collaboration could one day lead to the discovery of biomarkers which would give real insight into the clinical applications of the work presented in this thesis.

7 References

[1] Li, X., Du, E., Dao, M., Suresh, S. and Karniadakis, G.E., 2017. Patient-specific modeling of individual sickle cell behavior under transient hypoxia. PLoS computational biology, 13(3), p.e1005426.

[2] Blakely, I.P. and Horton, R.E., 2020. A microfluidic computational fluid dynamics model for cellular interaction studies of sickle cell disease vaso-occlusions. Microvascular Research, 132, p.104052.

[3] Li, X. and Lei, H., 2020. Multiscale Modeling of Sickle Cell Anemia. Handbook of Materials Modeling: Applications: Current and Emerging Materials, pp.2649-2666.

[4] Lei, H. and Karniadakis, G.E., 2013. Probing vasoocclusion phenomena in sickle cell anemia via mesoscopic simulations. Proceedings of the National Academy of Sciences, 110(28), pp.11326-11330.

[5] Zhang, X., Caruso, C., Lam, W.A. and Graham, M.D., 2020. Flow-induced segregation and dynamics of red blood cells in sickle cell disease. Physical review fluids, 5(5), p.053101.

[6] Dzwinel, W., Boryczko, K. and Yuen, D.A., 2003. A discrete-particle model of blood dynamics in capillary vessels. Journal of colloid and interface science, 258(1), pp.163-173.

[7] Recktenwald, S.M., Graessel, K., Maurer, F.M., John, T., Gekle, S. and Wagner, C., 2022. Red blood cell shape transitions and dynamics in time-dependent capillary flows. Biophysical Journal, 121(1), pp.23-36.

[8] Einstein, A, 1906. Viscosity of Solutions.

[9] Brown, E., Zhang, H., Forman, N.A., Maynor, B.W., Betts, D.E., DeSimone, J.M. and Jaeger, H.M., 2011. Shear thickening and jamming in densely packed suspensions of different particle shapes. Physical Review E, 84(3), p.031408.

[10] Mueller, S., Llewellin, E.W. and Mader, H.M., 2011. The effect of particle shape on suspension viscosity and implications for magmatic flows. Geophysical Research Letters, 38(13).

[11] Kato, G.J., Piel, F.B., Reid, C.D., Gaston, M.H., Ohene-Frempong, K., Krishnamurti, L., Smith, W.R., Panepinto, J.A., Weatherall, D.J., Costa, F.F. and Vichinsky, E.P., 2018. Sickle cell disease. Nature reviews Disease primers, 4(1), pp.1-22.

[12] Batchelor, G.K. and Green, J., 1972. The determination of the bulk stress in a suspension of spherical particles to order c2. Journal of Fluid Mechanics, 56(3), pp.401-427.

[13] Wyart, M. and Cates, M.E., 2014. Discontinuous shear thickening without inertia in dense non-Brownian suspensions. Physical review letters, 112(9), p.098302.

[14] Takeishi, N., Yamashita, H., Omori, T., Yokoyama, N., Wada, S. and Sugihara-Seki, M. (2022) "Inertial migration of red blood cells under a Newtonian fluid in a circular channel," Journal of Fluid Mechanics. Cambridge University Press, 952, p. A35. doi: 10.1017/jfm.2022.936.

[15] Makis, A.C., Hatzimichael, E.C. and Bourantas, K.L., 2000. The role of cytokines in sickle cell disease. Annals of hematology, 79, pp.407-413.

[16] Di Caprio, G., Schonbrun, E., Gonçalves, B.P., Valdez, J.M., Wood, D.K. and Higgins, J.M., 2019. High-throughput assessment of hemoglobin polymer in single red blood cells from sickle cell patients under controlled oxygen tension. Proceedings of the National Academy of Sciences,116(50), pp.25236-25242.

[17] Song, D., Gupta, R.K. and Chhabra, R.P., 2011. Drag on a sphere in Poiseuille flow of shear-thinning power-law fluids. Industrial engineering chemistry research, 50(23), pp.13105-13115.

[18] Herrick, J.B., 1910. Peculiar elongated and sickle-shaped red blood corpuscles in a case of severe anemia. Archives of internal medicine, 6(5), pp.517-521.

[19] Chebbi, R., 2015. Dynamics of blood flow: modeling of the Fåhræus–Lindqvist effect. Journal of biological physics, 41, pp.313-326.

[20] Fedosov, D.A., Peltomäki, M. and Gompper, G., 2014. Deformation and dynamics of red blood cells in flow through cylindrical microchannels. Soft matter, 10(24), pp.4258-4267.

[21] Abreu, D. and Seifert, U., 2013. Noisy nonlinear dynamics of vesicles in flow. Physical Review Letters, 110(23), p.238103.

[22] http://brennen.caltech.edu/fluidbook/basicfluiddynamics/Navierstokesexactsolutions/poiseuilleflow.pdf (accessed 27th July 2023)

[23] Kaoui, B., Biros, G. and Misbah, C., 2009. Why do red blood cells have asymmetric shapes even in a symmetric flow?. Physical review letters, 103(18), p.188101.

[24] Brenner, H., 1958. Dissipation of energy due to solid particles suspended in a viscous liquid. The Physics of Fluids, 1(4), pp.338-346.

[25] Krüger, T. ed., 2012. Computer simulation study of collective phenomena in dense suspensions of red blood cells under shear. Springer Science Business Media.

[26] Krüger, T., Varnik, F. and Raabe, D., 2011. Efficient and accurate simulations of deformable particles immersed in a fluid using a combined immersed boundary lattice Boltzmann finite element method. Computers Mathematics with Applications, 61(12), pp.3485-3505.

[27] Kaoui, B., Tahiri, N., Biben, T., Ez-Zahraouy, H., Benyoussef, A., Biros, G. and Misbah, C., 2011. Complexity of vesicle microcirculation. Physical Review E, 84(4), p.041906.

[28] Krüger, T., Gross, M., Raabe, D. and Varnik, F., 2013. Crossover from tumbling to tank-treading-like motion in dense simulated suspensions of red blood cells. Soft Matter, 9(37), pp.9008-9015.

[29] Kanter, J. and Falcon, C., 2021. Gene therapy for sickle cell disease: where we are now?. Hematology, 2021(1), pp.174-180.

[30] Eaton, W.A., 2020. Hemoglobin S polymerization and sickle cell disease: A retrospective on the occasion of the 70th anniversary of Pauling's Science paper. American journal of hematology,

95(2), pp.205-211.